

## CALL FOR PAPERS | *Neuronal Diversity: Categorizing Types of Neurons*

### Categorically distinct types of receptive fields in early visual cortex

Vargha Talebi and Curtis L. Baker, Jr.

McGill Vision Research, Department of Ophthalmology, McGill University, Montreal, Quebec, Canada

Submitted 2 July 2015; accepted in final form 29 February 2016

**Talebi V, Baker CL Jr.** Categorically distinct types of receptive fields in early visual cortex. *J Neurophysiol* 115: 2556–2576, 2016. First published March 2, 2016; doi:10.1152/jn.00659.2015.—In the visual cortex, distinct types of neurons have been identified based on cellular morphology, response to injected current, or expression of specific markers, but neurophysiological studies have revealed visual receptive field (RF) properties that appear to be on a continuum, with only two generally recognized classes: simple and complex. Most previous studies have characterized visual responses of neurons using stereotyped stimuli such as bars, gratings, or white noise and simple system identification approaches (e.g., reverse correlation). Here we estimate visual RF models of cortical neurons using visually rich natural image stimuli and regularized regression system identification methods and characterize their spatial tuning, temporal dynamics, spatiotemporal behavior, and spiking properties. We quantitatively demonstrate the existence of three functionally distinct categories of simple cells, distinguished by their degree of orientation selectivity (isotropic or oriented) and the nature of their output nonlinearity (expansive or compressive). In addition, these three types have differing average values of several other properties. Cells with nonoriented RFs tend to have smaller RFs, shorter response durations, no direction selectivity, and high reliability. Orientation-selective neurons with an expansive output nonlinearity have Gabor-like RFs, lower spontaneous activity and responsivity, and spiking responses with higher sparseness. Oriented RFs with a compressive nonlinearity are spatially nondescript and tend to show longer response latency. Our findings indicate multiple physiologically defined types of RFs beyond the simple/complex dichotomy, suggesting that cortical neurons may have more specialized functional roles rather than lying on a multidimensional continuum.

visual cortex; receptive field; cell types; system identification; natural images

RECEPTIVE FIELD (RF) properties of early visual cortex neurons are fundamentally important to achieving an understanding of early visual signal processing—in particular, to understand how details of visual images are represented by neuronal signals, for example, in extraction of simple features or in efficient coding of natural images (NIs). RF properties may also be suggestive of underlying neural circuitry, e.g., neurons with simple properties might serve as a substrate for construction of selectivity for more complex features. In general, comparison of RF properties in different cortical areas can help elucidate differences in overall functionality of those areas.

Early visual cortex neurons are widely viewed as lying on a multidimensional continuum of RF properties such as optimal

orientation or spatial frequency (SF). The only generally recognized categorical types have been simple and complex cells, based on segregation of excitatory and inhibitory zones (Hubel and Wiesel 1959) or degree of response modulation by gratings (Skottun et al. 1991). The apparent lack of physiological categories of cortical neurons might seem consistent with the idea that because of the extreme connectivity (“random wiring”) of cortical circuitry (Chklovskii 2004) each neuron would show some physiological attributes of many others, but most previous studies of visual cortex neurons have used very simple, stereotyped stimuli such as bars, sine wave gratings, or white noise (WN), which might fail to reveal important RF properties. Another limitation of previous studies may have been the widespread use of manually controlled, bar-shaped “search stimuli” to look for responsive neurons, which could have introduced sampling biases (Olshausen and Field 2005).

Here we employ visually rich NI stimuli to activate visual neurons in cat Area 18 (A18) and estimate spatiotemporal receptive field (STRF) using system identification with regularized regression methods (Wu et al. 2006). RF estimates derived from NI stimuli can more accurately predict neural responses to other types of visual stimuli (Felsen et al. 2005; Talebi and Baker 2012). Additionally, NIs may drive neurons at a more ecologically relevant operating point, potentially revealing important distinguishing properties of neural responses (David et al. 2004; Felsen and Dan 2005). Here we also utilize multielectrode recording with post hoc spike sorting, without reliance on prior use of search stimuli to isolate single neurons. We concentrate our analysis on simple cells, which have significant linear response components and are therefore amenable to our analysis [linear-nonlinear (LN) model architecture; see METHODS]. We sample neurons in A18 primarily because our long-term objectives are to understand second-order processing (Mareschal and Baker 1998), which is more prevalent in cat A18 than in Area 17 (A17) (Zhou and Baker 1994), and more generally because there may be greater scope in a secondary cortical area for NI stimuli to reveal more complex processing (e.g., Hegde and Van Essen 2000).

Quantitative analysis of the estimated RFs reveals a greater diversity of RF properties than previously described. We are able to distinguish three kinds of simple-type cells, distinguished by their degree of orientation selectivity and the nature of their output nonlinearity. The three cell types also differ from one another in optimal SF, temporal dynamics, direction selectivity, and spiking properties. These results challenge the prevailing idea that early cortical neurons operate across an amorphous continuum. Instead, physiological response prop-

Address for reprint requests and other correspondence: C. L. Baker, Jr., McGill Vision Research, Dept. of Ophthalmology, 1650 Cedar Ave., Rm. L11.112, Montreal, QC, Canada H3G 1A4 (e-mail: curtis.baker@mcgill.ca).

erties are categorically distinct, implying that visual cortex neurons have specialized functional roles.

## METHODS

**Animal preparation.** Anesthesia was induced by isoflurane-oxygen (3–5%) inhalation, followed by intravenous (iv) cannulation and bolus iv injection of thiopental sodium (8 mg/kg) or propofol (5 mg/kg). Surgical anesthesia was maintained with supplemental doses of thiopental sodium or propofol. Atropine sulfate (0.05 mg/kg iv) or glycopyrrolate (30  $\mu\text{g}$  im) and dexamethasone (0.2 mg/kg iv or 1.8 mg im) were administered and a tracheal cannula or intubation tube inserted. Throughout the surgery, body temperature was thermostatically maintained and heart rate was monitored (Vet/Ox Plus 4700).

The animal was then positioned in a stereotaxic apparatus and connected to a respirator (Ugo Basile 6025). In early experiments, pentobarbital sodium (1.0  $\text{mg}\cdot\text{kg}^{-1}\cdot\text{h}^{-1}$ ) was administered after a bolus injection to effect. In later experiments, propofol (5.3  $\text{mg}\cdot\text{kg}^{-1}\cdot\text{h}^{-1}$ ) was supplemented with fentanyl citrate (7.4  $\mu\text{g}\cdot\text{kg}^{-1}\cdot\text{h}^{-1}$ ) after a bolus injection (2.5  $\mu\text{g}/\text{kg}$ ). Both anesthesia regimes were further supplemented with oxygen-nitrous oxide (70:30), and a continuous infusion of lactated dextrose-saline (2 ml/h iv) was supplied. A craniotomy (A3/L4) over cortical A18 was performed, followed by a small durotomy. The cortical surface was protected with 2% agarose capped with petroleum jelly. Paralysis was produced with a bolus iv injection of gallamine triethiodide (to effect), followed by infusion (10  $\text{mg}\cdot\text{kg}^{-1}\cdot\text{h}^{-1}$ ). Local injections of bupivacaine (0.50%) were administered at all surgical sites. Expired  $\text{CO}_2$ , EEG, ECG, body temperature, blood oxygen, heart rate, and airway pressure were monitored and maintained at appropriate levels.

Corneas were initially protected with topical carboxymethylcellulose (1%) and subsequently with neutral contact lenses. Spectacle lenses were selected with slit retinoscopy to produce emmetropia at 57 cm, and artificial pupils (2.5 mm) were provided.

Daily maintenance included topical atropine sulfate (1%) and phenylephrine hydrochloride (2.5%), as well as intramuscular glycopyrrolate (16  $\mu\text{g}$ ) and dexamethasone (1.8 mg). All animal procedures were approved by the McGill University Animal Care Committee and are in accordance with the guidelines of the Canadian Council on Animal Care.

**Stimuli.** Visual patterns were generated on a Macintosh computer (MacPro, 2.66 GHz Quad Core Intel Xeon, 6 GB, NVIDIA GeForce GT 120) with custom software written in MATLAB (MathWorks) and the Psychophysics Toolbox (Brainard 1997; Kleiner et al. 2007) and displayed on a gamma-corrected CRT monitor (NEC FP1350, 20 in.,  $640 \times 480$  pixels, 75 Hz, 36  $\text{cd}/\text{m}^2$ ) at a viewing distance of 57 cm.

Broadband NI stimuli were constructed from  $480 \times 480$ -pixel monochrome portions of high-quality digital photographs (Olmos and Kingdom 2004). Nearly blank images (e.g., sky, water) were rejected by setting a root mean square energy threshold. Remaining images were root mean square-normalized with mean luminance equated for each image. Images were assembled into stimulus ensembles, consisting of 375 images presented as 5-s movies. In some cases (21 of 212) each image was presented for two frames, to drive a stronger response.

**Electrophysiology.** Extracellular recordings were obtained with single-channel, glass-coated platinum-iridium or Parylene-coated tungsten microelectrodes (Frederick Haer) and silicon linear-array multielectrodes (NeuroNexus A1 $\times$ 16 or A1 $\times$ 32) or multishank tetrodes (NeuroNexus A4 $\times$ 1-tet) with 177- $\mu\text{m}^2$  pad sizes. Electrode penetrations were made approximately perpendicular to the brain surface, yielding similar RF locations for recording sites along the length of a linear-array multielectrode. Electrodes were advanced with a stepping motor microdrive (M. Walsh Electronics, uD-800A). A primary, single-channel recording pathway incorporated an audio monitor, a window discriminator (Frederick Haer) to isolate single units, and a delay-triggered oscilloscope to monitor isolation. Spike times were recorded at

a resolution of 100  $\mu\text{s}$  (Instrutech, ITC-18) and time-referenced to the stimulus with an optical photo sensor (TAOS T2L 12S) placed on a corner of the CRT monitor containing stimulus timing information. A secondary, parallel, multichannel recording pathway (Plexon Recorder, version 2.3) acquired broadband raw signals for up to 32 channels at 40 kHz and stored them to hard disk for subsequent spike sorting and detailed analysis. One of the channels was also routed to the primary recording pathway for online analysis to guide the recording protocol.

For single-channel electrodes, or in some cases for a selected site of a multielectrode, manually controlled bar-shaped stimuli were used to assess the approximate location, orientation preference, and ocular dominance of isolated neurons or of multiunit activity. Recorded cells had eccentricities ranging from 5° to 30°. The CRT monitor was centered accordingly, and all subsequent stimuli were presented monocularly to the dominant eye. Single isolated neurons were first characterized with conventional tuning curve measurements using sine wave grating patterns to determine optimal SF, orientation, and temporal frequency. The cell's RF was further localized by displaying small grating patches at a grid of spatial locations, and the monitor was repositioned as necessary.

NI ensembles were then presented, with three independent data sets collected for training, regularization, and validation (Fig. 1), each requiring ~20–30 min. The training stimuli consisted of 20 image ensembles (total of 7,500 unique images), each repeated 5 times. The regularization and validation stimuli each consisted of 5 image ensembles (1,875 unique images each), each repeated 20 times. This trade-off of stimulus diversity vs. repetitions was aimed at maximizing the informativeness provided by unique images (training) but minimizing average response variance (regularization, validation).

Responses from a total of 508 neurons were collected in 26 adult cats of either sex. Additional data were also collected during these recording sessions as part of other ongoing projects in the same laboratory.

**Data analysis: estimation of receptive field models.** In experiments in which raw neuronal data were recorded, spike waveform signals were sorted post hoc with Plexon Offline Sorter (Plexon, version 3.2.3). Single units were carefully classified manually with conservative thresholds for clear separation of distinct signals.

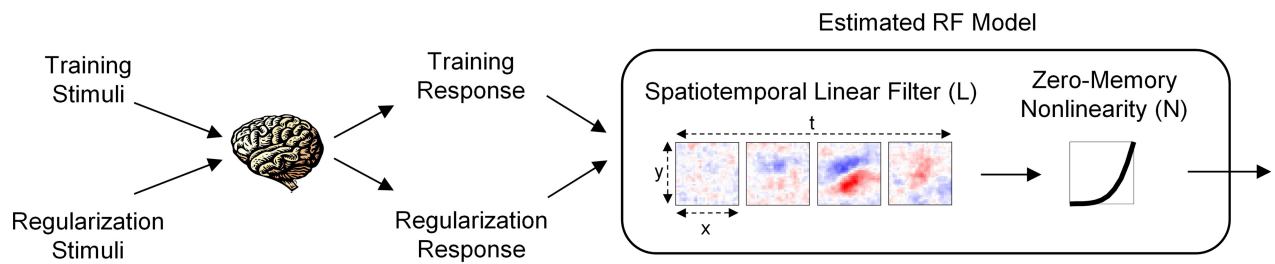
Neurons were classified as simple or complex based on the degree of firing rate modulation by an optimal drifting grating (Skottun et al. 1991) or the presence of distinct excitatory and inhibitory subregions in the estimated RF maps. Only simple-type cells having a sufficient response (see below) to our stimuli ( $N = 212$ ) were used for subsequent analysis.

The NI ensembles were normalized to have zero mean and unity standard deviation for the entire stimulus matrix. Stimulus images ( $480 \times 480$ ) were cropped with a square window designed to efficiently encompass the RF and downsampled to  $32 \times 32$ . The cropping window was selected by an unsupervised procedure based on the width of the best-fitting two-dimensional (2D) Gaussian or Gabor function applied to a low-resolution estimate of the spatial RF at the peak lag; in a minority of cases in which this procedure failed, the window was determined by manual inspection.

Spike times were collected into poststimulus time histograms binned at the stimulus refresh rate (i.e., bin width 13.3 ms), which were averaged across repetitions and normalized to have zero mean and unity standard deviation for the entire response. For cells producing average spike frequencies  $< 1$  spike/s the gradient descent algorithm (see below) generally failed to converge, and these cells (~10% of the total sample) were omitted from further analysis. Our resultant sample included 69 neurons from single-channel (Frederick Haer) electrodes, 132 from linear-array multielectrodes (NeuroNexus A1 $\times$ 16 or A1 $\times$ 32), and 11 from multishank tetrodes (NeuroNexus A4 $\times$ 1-tet).

Each neuron's RF model was estimated within the framework of a generalized linear model, consisting of a linear STRF and a zero-

## A Model Estimation



## B Model Evaluation

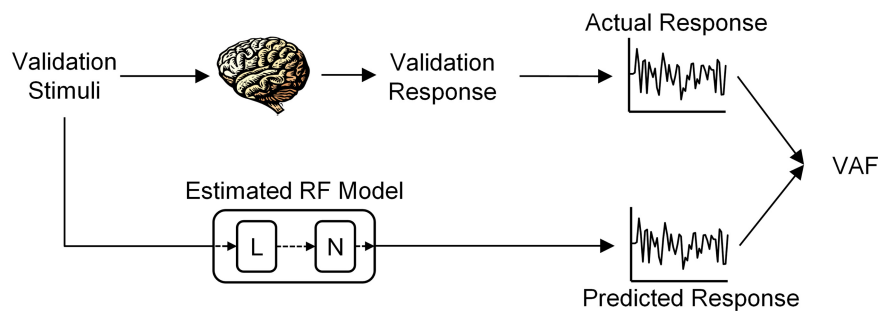


Fig. 1. System identification procedure. Neural responses of simple-type cells to natural image stimuli were used to estimate receptive field (RF) models and evaluate their predictive robustness. *A*: RF model estimation. Training and regularization data sets (i.e., stimuli and responses) were used to estimate a 3-dimensional [space ( $x$ )-space ( $y$ )-time ( $t$ )] spatiotemporal receptive field (STRF), modeled as a linear (L) filter. A subsequent zero-memory nonlinearity (N) was fit from comparison with measured responses. L and N together make up the estimated RF model. *B*: RF model evaluation. The estimated RF model's response to a separate set of validation stimuli provides a predicted response, which was compared with the actual (measured) validation response. The quality of prediction was quantified by the percentage of measured response variance accounted for (VAF) by the predicted response.

memory nonlinearity (ZMN; Fig. 1A) (Wu et al. 2006), with the *strflab* toolbox for MATLAB (Oliver 2010). Further details of the model architecture and its estimation and evaluation may be found in our earlier paper (Talebi and Baker 2012). In brief, neuronal responses to training stimuli were used to estimate the pixel “weights” of the linear STRF. The weights were optimized with iterative gradient descent to minimize the mean square error between the responses of the model and those in the training data set. To circumvent overfitting, regularization was implemented with early stopping (Hagiwara 2002; Willmore et al. 2010)—the gradient descent was halted when further iterations failed to produce improvements in the ability of the trained model to predict the regularization data set. The ZMN was modeled as a half-wave rectified power law, whose exponent was fit (with MATLAB'S *fminsearch*) to a plot of measured training responses vs. predicted values based on the estimated STRF.

Responses to a novel set of validation stimuli were used to assess the predictive ability of the estimated RF model (Fig. 1B). The validation stimuli were convolved with the STRF and put through the ZMN to produce a predicted response that was compared with the actual validation response. The predictive accuracy was quantified as “raw variance accounted for” (raw VAF), which is the square of the correlation coefficient expressed as a percentage. In practice, the raw VAF would never reach 100%, since neural responses are very noisy and the RF model undoubtedly fails to capture other nonlinearities not instantiated in the model architecture. To address this issue we used a noise ceiling analysis (David and Gallant 2005; Talebi and Baker 2012) that incrementally increases the amount of data used to train and validate the estimated STRF. This “explainable” VAF provides an estimate of the fraction of total response that could theoretically be predicted in the absence of neural noise. The

estimated RF models used here produced reasonable levels of predictive power (average raw VAF 20%, explainable VAF 41%) for useful consideration of RF properties.

All of these data analysis procedures were extensively validated by testing on both hardware (Li et al. 2010) and software models.

*Data analysis: characterization of RF models.* Orientation and SF selectivity were assessed at the peak lag (temporal lag with highest average variance). The spatial RF at that lag (Fig. 2A) was multiplied by a Gaussian window and zero-padded to reduce high-frequency edge effects in the Fourier transform. The magnitude part of the 2D FFT (Fig. 2B) was converted to a plot of amplitude as a function of SF and orientation (Fig. 2C). Note that the two peaks are not necessarily symmetrical, since they now represent opposite directions of motion. From this plot a one-dimensional orientation profile was extracted at the highest average SF (Fig. 2D). The orientation profile was characterized by a vector-based summation method to indicate orientation bias and optimal orientation (Leventhal et al. 2003; Worgotter and Eysel 1987):

$$OB = \left| \frac{\sum_k R_k e^{i2\theta_k}}{\sum_k R_k} \right| \quad (1)$$

$$O_{opt} = \arg \left( \frac{\sum_k R_k e^{i2\theta_k}}{\sum_k R_k} \right) \quad (2)$$

where  $R_k$  = response at stimulus orientation  $\theta_k$ ; OB = orientation bias; and  $O_{opt}$  = optimal orientation. OB values are dimensionless and have a bounded range between zero (no orientation selectivity) and unity (perfect selectivity).  $O_{opt}$  has a bounded range between  $0^\circ$

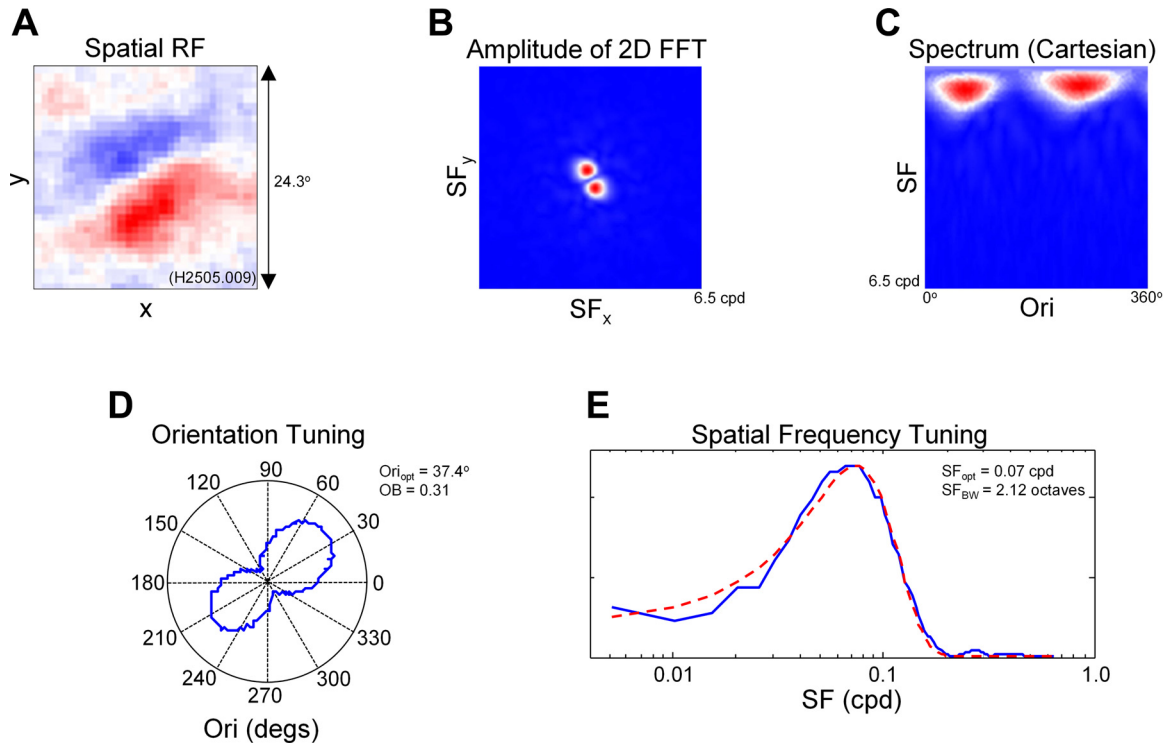


Fig. 2. Tuning parameters. Procedure for extracting orientation and spatial frequency (SF) tuning parameters from spatial receptive fields (RFs). *A*: the spatial RF at peak latency is extracted from the spatiotemporal receptive field (STRF). *B*: the magnitude part of the 2D Fourier transform (FFT) (i.e., amplitude spectrum) is computed and frequency shifted so SF components are symmetrical about the origin. *C*: the polar representation of the amplitude spectrum is converted to Cartesian coordinates, resulting in a plot of amplitude as a function of SF and orientation (Ori). The global peak value of this plot was used to construct transects (dashed lines) for orientation and spatial tuning profiles. *D*: taking a profile along the Ori axis (y-axis) at peak SF in *C* results in an orientation tuning curve, which is parameterized by a vector summation method. This example cell has an optimal orientation ( $Ori_{opt}$ ) of  $37.4^\circ$  and orientation bandwidth (OB) of 0.31. *E*: taking a profile along the SF axis at peak Ori in *C* results in a SF tuning curve. This example cell has an optimal SF ( $SF_{opt}$ ) of 0.07 cycles/° and a SF bandwidth ( $SF_{BW}$ ) of 2.12 octaves. Dashed red line represents the fitted Gaussian function according to Eq. 3.

and  $180^\circ$ . Cells with orientation bias values  $> 0.1$  are considered to be orientation sensitive (Leventhal et al. 2003).

As an alternative measure of orientation selectivity, we fitted the tuning curves with a von Mises function (Batschelet 1981; Swindale 1998):

$$R(\theta) = ke^{w[\cos 2(\theta - O_{opt}) - 1]} \quad (3)$$

where  $R(\theta)$  = response at stimulus orientation  $\theta$ ;  $k$  = maximum response amplitude;  $O_{opt}$  = optimal orientation; and  $w$  = a width parameter indicative of orientation bandwidth.

The SF tuning curve (Fig. 2E) was similarly determined by extracting a SF profile at peak average orientation. This SF tuning curve was fit with a Gaussian function to yield estimates of SF bandwidth and optimal SF (DeAngelis et al. 1994):

$$R(sf) = ke^{-\left(\frac{sf - SF_{opt}}{\alpha}\right)^2} + R_0 \quad (4)$$

where  $k$  = maximum response amplitude;  $sf$  = measured SF in cycles/°;  $SF_{opt}$  = optimal SF;  $1.65\alpha$  = full width at half-maximum (FWHM) tuning bandwidth in octaves;  $R_0$  = spontaneous response; and  $R(sf)$  = fitted response as a function of SF (shown as the dashed red line in Fig. 2E).  $k$ ,  $SF_{opt}$ ,  $\alpha$ , and  $R_0$  were the free parameters of the fitted function. We employed a parametric approach to characterize SF tuning curves because they all have very similar shapes for visual cortex neurons, and therefore all could be fit accurately with the same function. In other cases where the shape of the response function is highly variable from one neuron to another (below), we instead employ nonparametric approaches.

To assess whether the spatial RF at peak lag was dominated by excitatory (ON) or by inhibitory (OFF) regions, a “zero balance index” (ZBI) was calculated:

$$ZBI = \frac{\sum w_{pos} - |\sum w_{neg}|}{\sum w_{pos} + |\sum w_{neg}|} \quad (5)$$

where  $\sum w_{pos}$  = sum of all positive-valued linear filter weights and  $|\sum w_{neg}|$  = absolute value of the sum of all negative-valued linear filter weights. The ZBI ranged from  $-1$  to  $1$ , with  $0$  representing a balanced spatial RF, a positive number an ON-dominated spatial RF, and a negative number an OFF-dominated spatial RF.

The neuron’s temporal profile and spatial aspect ratio were quantified by creating a variance map of the STRF (Fig. 3A) (Malone et al. 2007; Xing et al. 2009; Zheng and Yao 2012). (Note that Gabor curve fits were not used because many STRFs were orientationally isotropic and thus not well fit by Gabor functions). The first noncausal lag was included as part of the STRF estimation, and the mean of its variance was used as a measure of the baseline noise and subtracted from the variance of the STRF estimate:

$$\text{Var}_{map}(i, j, k) = w(i, j, k)^2 - \overline{c(i, j)^2} \quad (6)$$

where  $w(i, j, k)$  = weight of  $i, j$ th pixel and  $k$ th time index of the STRF;  $c(i, j)$  = noncausal RF estimate at  $i, j$ th pixel; and  $\text{Var}_{map}(i, j, k)$  = variance map of the STRF at  $i, j$ th pixel and  $k$ th time index.

Averaging the variance map spatially at each lag resulted in the temporal profile of the neuron’s response (Fig. 3B). The average variances at each lag were fit with a piecewise polynomial form of a cubic spline interpolation (MATLAB’S *spline*), in order to extract the time to peak response (response latency, RL) and the width of the temporal envelope (response duration, RD). RL was measured as the time at which the interpolating spline reached maximum value. RD was computed between the levels that were  $1/e$  of the peak envelope value (DeAngelis et al. 1993).

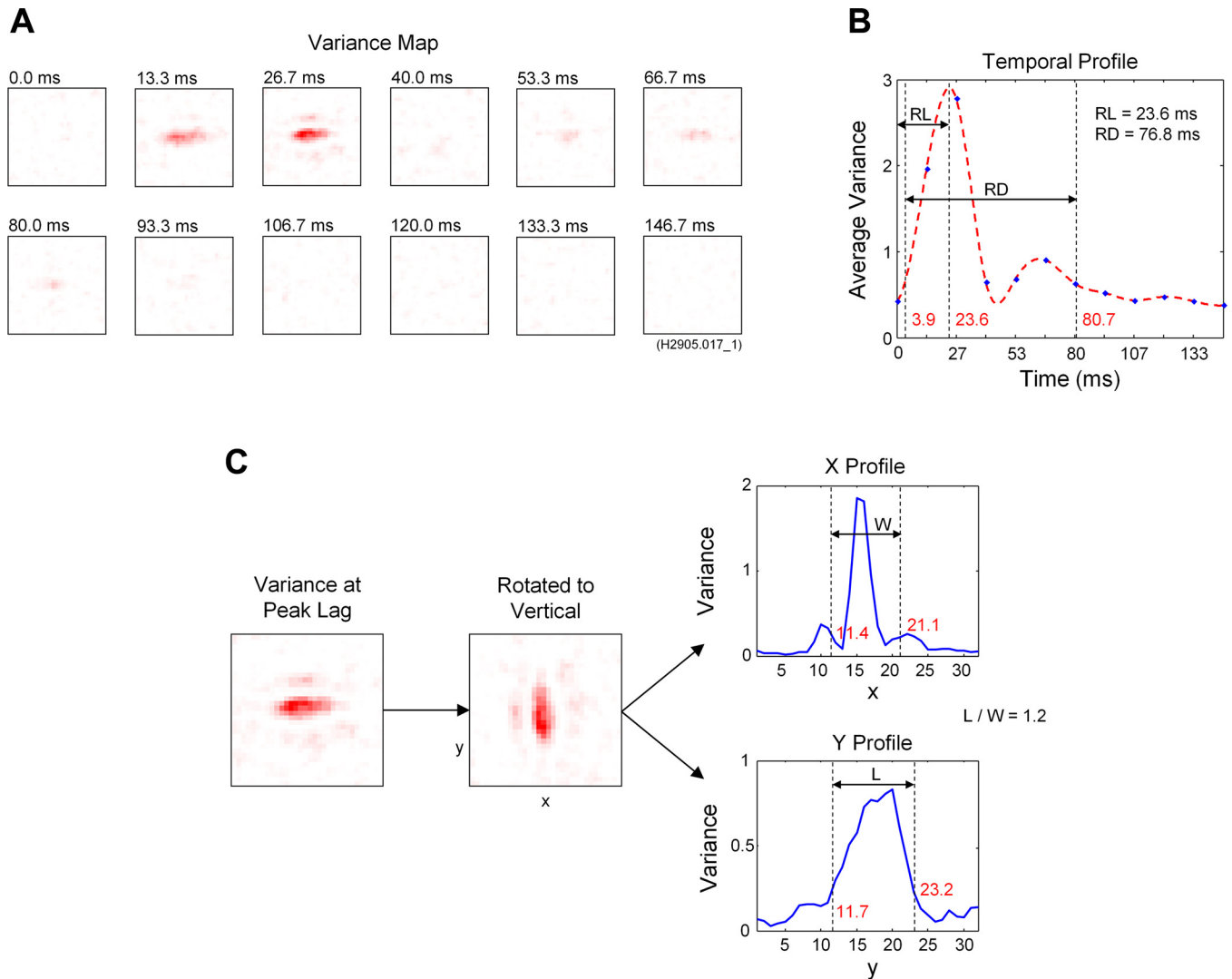


Fig. 3. Variance maps. Nonparametric procedure to extract temporal and spatial properties. *A*: variance map computed from the estimated spatiotemporal receptive field (STRF). *B*: average variance of STRF at each time lag results in a temporal profile. blue points are the average variance at each lag, and red dashed line is a fitted spline. Response latency (RL) is taken as the latency to the peak of the fitted spline. Response duration (RD) is taken as the duration between thresholds of  $1/e$  times the peak value. In this example, RL = 23.6 ms and RD = 76.8 ms. *C*: variance map at peak latency is used to determine the spatial profile. Rotating the peak variance map to vertical and then averaging along the  $y$ -axis results in a  $X$  profile, while averaging along the  $x$ -axis results in a  $Y$  profile. The width ( $W$ ) and length ( $L$ ) are determined by computing the weighted means and standard deviations of the  $X$  and  $Y$  profiles, respectively. The length-to-width aspect ratio of this example cell is  $L/W = (23.2 - 11.7)/(21.1 - 11.4) = 1.2$ .

To estimate the aspect ratio of the neuron’s RF (Fig. 3C), the spatial variance map at peak lag was rotated to a vertical orientation with principal component analysis. Since the peak spatial variance map is 2D, there are two principal components, with the first following the direction of maximum variance (length) and the second being orthogonal to it (width). The ratio of the first principal component’s column elements is the slope of the principal axis, whose angle with respect to the vertical corresponds to the rotation angle. Averaging across the length yields an  $X$  profile (i.e., a 1-dimensional representation of the RF’s spatial width), while averaging across the width yields a  $Y$  profile (i.e., length). To determine each neuron’s aspect ratio, the centroids of the  $X/Y$  profiles were first calculated as weighted means:

$$\bar{x}_w = \frac{\sum w_i x_i}{\sum w_i} \tag{7}$$

$$\bar{y}_w = \frac{\sum w_i y_i}{\sum w_i} \tag{8}$$

where in Eq. 7  $w_i$  is the corresponding length-averaged linear filter weights for each observation  $x_i$  and  $\bar{x}_w$  is the centroid along the  $x$ -axis. Similarly in Eq. 8,  $w_i$  is the corresponding width-averaged linear filter weights for each observation in  $y_i$  and  $\bar{y}_w$  is the centroid along the  $y$ -axis. The width ( $W$ ) and length ( $L$ ) of the  $X$  and  $Y$  profiles were then calculated as

$$W = 2 \times \sigma_x = 2 \times \sqrt{\frac{\sum w_i (x_i - \bar{x}_w)^2}{(n - 1) \sum w_i}} \tag{9}$$

$$L = 2 \times \sigma_y = 2 \times \sqrt{\frac{\sum w_i (y_i - \bar{y}_w)^2}{(n - 1) \sum w_i}} \tag{10}$$

where  $\sigma_x$  and  $\sigma_y$  = weighted standard deviations along the width and length, respectively, and  $n$  = total number of weights along the

profiles. The spatial aspect ratio was then taken as the maximum of the dimensions  $L$  and  $W$ , divided by their minimum.

A direction selectivity index (DSI) was calculated to indicate the degree of a neuron's space-time nonseparability that would give rise to direction selectivity (Fig. 4) (Baker 2001; DeAngelis et al. 1993). A three-dimensional STRF estimate was rotated to vertical (Fig. 4A) using the rotation angle calculated from principal component analysis (as above). Taking the mean along the RF's length, for each lag, then upsampling, resulted in a square 2D space ( $x$ )-time ( $t$ ) RF (Fig. 4B). The magnitude part of its Fourier transform was frequency shifted (Fig. 4C), with the upper quadrants representing the responses in the preferred and null directions (because of symmetry, the bottom quadrants were redundant). The DSI was calculated as

$$\text{DSI} = \frac{R_p - R_n}{R_p + R_n} \quad (11)$$

where  $R_p$  = preferred direction response, taken as the peak value in *quadrant 1*, and  $R_n$  = null direction response, taken as the value in *quadrant 2* at the same spatial and temporal frequency of  $R_p$ . The upper quadrants were flipped along the vertical as needed to always place  $R_p$  in *quadrant 1*, since here we are interested in the amount of direction selectivity and not its preferred direction. The DSI has a

bounded range between 0 and 1, where 0 is entirely non-direction-selective (i.e., space-time separable) and 1 is perfectly direction-selective (i.e., space-time nonseparable). It is important to note that although a separable filter would not produce direction selectivity and a nonseparable filter would be selective for direction of motion (Reid et al. 1991), the DSI is not a completely general index of spatiotemporal nonseparability as such. It applies only to the particular kind of space-time nonseparability related to a spatiotemporally linear mechanism of direction selectivity.

*Data analysis: spiking responses and spike waveforms.* Several measures of spiking response properties were measured for each neuron. Spontaneous activity was measured by counting the number of spikes that occurred during the 1-s mean luminance blank screen that preceded each stimulus ensemble. Responsivity was taken as the average number of spikes that occurred during stimulus presentation minus the average spontaneous activity. Both of these measurements were averaged across all repetitions of all stimulus ensembles used for all three data sets (training, regularization, validation) on each neuron.

As an indicator of the lifetime sparseness of a neuron's firing, we employed a measure of the neuron's stimulus selectivity (Lesica et al. 2007; Vinje and Gallant 2002). This sparseness index (SI) was calculated as

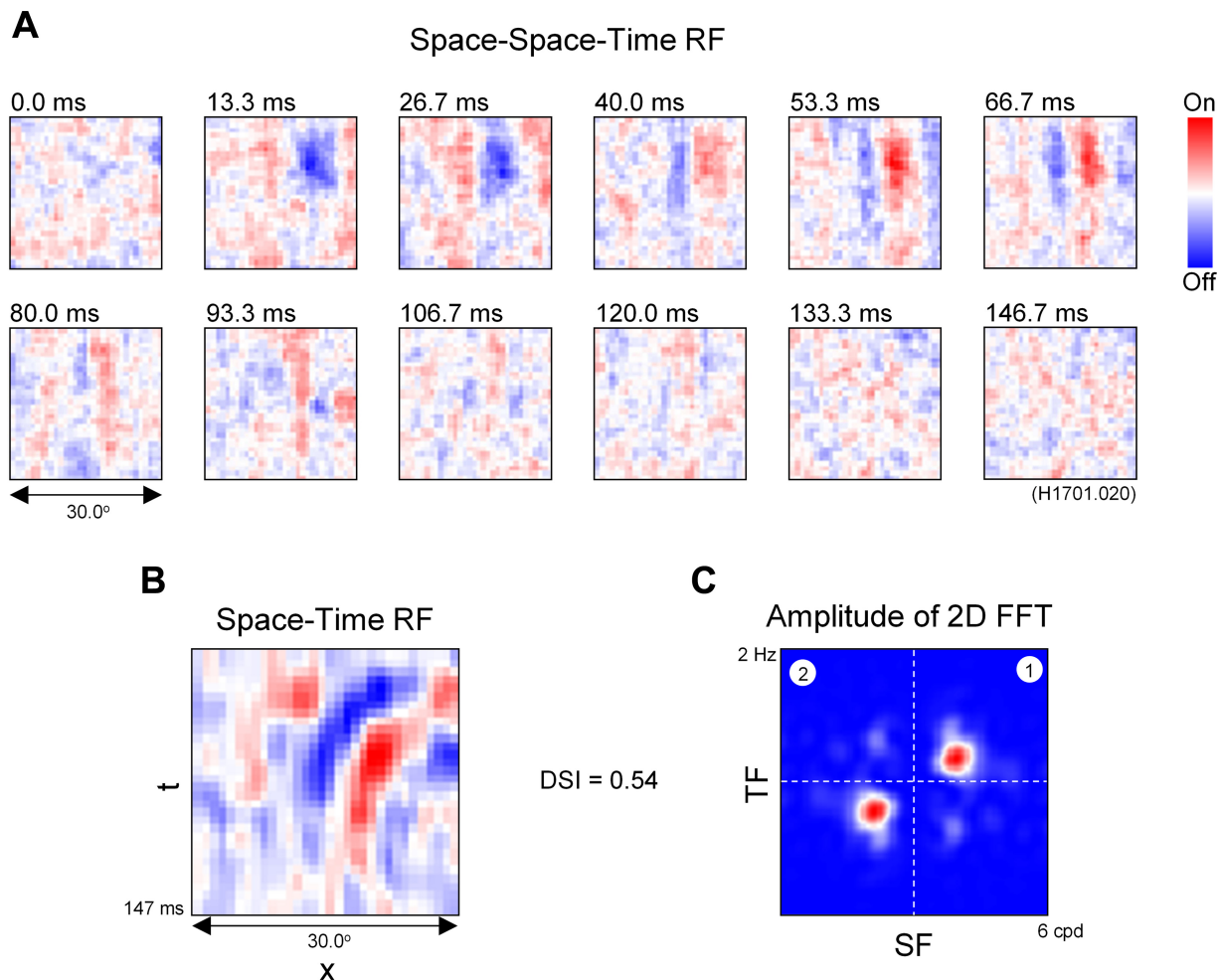


Fig. 4. Direction selectivity. Procedure for determining a direction selectivity index (DSI), which can be used to infer the degree of space-time separability that would give rise to direction-selective responses. *A*: a full space-space-time RF for an example cell, rotated to a vertical orientation, showing a leftward phase progression across time lags. *B*: averaging across 1 spatial dimension (i.e., along  $y$ ) results in a 2D RF (space  $x$ , time  $t$ ). *C*: the magnitude part of the 2D Fourier transform (i.e., amplitude spectrum) of *B*, as a function of temporal frequency (TF) and spatial frequency (SF). Dashed white lines represent the boundaries of the quadrants, with preferred direction in the *top right* (1) and nonpreferred in the *top left* (2). In this example, the cell has a DSI = 0.54.

$$SI = \frac{1 - \mu^2 / (\mu^2 + \sigma^2)}{1 - 1/n} \quad (12)$$

where  $\mu$  = mean response,  $\sigma$  = standard deviation of response, and  $n$  = number of time bins. This index ranges from zero (equal response to all stimuli) to unity (response to only 1 stimulus image).

An index of the trial-to-trial reliability of a neuron's response to a given stimulus was calculated from a signal-to-noise ratio estimate (Borst and Theunissen 1999; Lesica et al. 2007). First the mean response to multiple repetitions of a stimulus ensemble was calculated, and its Fourier spectrum provided an estimate of the signal. Then for each trial the noise was taken as the difference between the ensemble mean response and the individual response, and the mean power spectrum of these noise functions provided the noise spectrum. The reliability index (signal-to-noise ratio) was the ratio of the total power in each of these spectra.

Spike widths were measured from spike waveforms (8 ms) exported from Plexon Offline Sorter, which were sampled at 31.25 kHz in 32-channel recordings and at 40 kHz in 16-channel or single-channel recordings. For comparison to different measures used in the literature, we took the FWHM and also the time from the waveform's maximum to its minimum ("peak to valley"). This analysis could only be performed for cells that were isolated with off-line spike sorting (for those obtained with a hardware window discriminator, only the times of detected spike events were recorded).

Population average values are reported as means  $\pm$  SE. Significance of pairwise comparisons was, unless noted, evaluated with unpaired Student's *t*-tests. Significance of histogram bimodality was assessed with the Hartigan dip test (Hartigan and Hartigan 1985).

**Cluster analysis.** To objectively determine whether there were multiple clusters of pairs of neuronal RF parameter values, and if so how many, a Gaussian mixture model (GMM) clustering algorithm (McLachlan and Basford 1988) was employed with MATLAB'S *gmdistribution.fit*. A Gaussian mixture distribution with specified number of components (i.e., clusters) was fit to the data with an expectation-maximization (EM) algorithm that constructs a maximum likelihood estimate of the parameters in the GMM. GMMs assume that data points are sampled from a mixture of a finite number of Gaussian distributions, each having its own mean (location) and covariance (shape). Each data point has a posterior probability assignment, indicating the probability of belonging to a specific cluster. Cluster membership is assigned by maximizing these posterior probabilities.

Akaike and Bayes information criteria (AIC and BIC, respectively) (Akaike 1974, 1998) were used to objectively determine the appropriate number of clusters in the GMM. These information criteria penalize models with too many additional parameters, thereby preventing overfitting. The candidate model that is most appropriate is the one with the lowest AIC/BIC value.

## RESULTS

Some representative examples of estimated RF models for simple cells are shown in Fig. 5. Each row depicts results for one cell, showing a STRF across eight time lags (0.0 ms to 93.3 ms), a fitted ZMN with the exponent ( $a$ ) of the power law nonlinearity, the orientation bias (OB) at peak lag, and the explainable VAF. In the first example (Fig. 5A), the RF map exhibited adjacent, elongated alternating ON and OFF regions, resembling a Gabor-like structure, which produced a strong orientation bias (OB = 0.31). There was a weak phase reversal at later time lags, and the ZMN was expansive, with a power law of 2.4. This example neuron had a RF structure and output nonlinearity that resemble those typically reported by other groups (Gardner et al. 1999) and is the basis for many popular models of early cortical RFs, e.g., Gabor filters followed by

half-squaring (Heeger 1992). Another example (Fig. 5B) had a horizontally oriented ON region and flanking OFF lobes (possibly with a slight crescent shape, as in Conway and Livingstone 2006), as well as strong orientation bias (OB = 0.25). The ZMN was expansive, with a power of 1.5.

Unlike the above examples, a substantial minority of cells had nonoriented RFs. For example, in Fig. 5C the cell had an ON-center, OFF-surround structure, no orientation selectivity (OB = 0.05), and a clear phase reversal at later time lags. The ZMN was expansive, with a power of 1.4. A somewhat noisier example (Fig. 5D) had a concentric, OFF-center/ON-surround STRF, no orientation selectivity (OB = 0.01), and a strong phase reversal at later time lags. The ZMN was expansive, with a power of 2.0. Nonoriented RFs have been previously reported in cat visual cortex (e.g., Dragoi et al. 2001; Hirsch et al. 2003; Martinez et al. 2005; see also discussion by Ringach et al. 2002), but we were surprised to encounter them so frequently (about one-third of the sample).

Other neurons exhibited less clearly stereotypical RF maps, with spatiotemporal structures that were more varied compared with the typical Gabor-like or center-surround structure of the above examples. In Fig. 5E, the RF map had adjacent horizontal ON and OFF regions and was orientation selective (OB = 0.33). Unlike the previous examples, the ZMN was compressive, with a value of 0.5. In Fig. 5F, the STRF had a somewhat nondescript spatial structure that was modestly orientation selective (OB = 0.19). The ZMN was also compressive, with a power law of 0.7. Most previous studies have reported expansive rather than compressive output nonlinearities of early cortical neurons (but see Xing et al. 2011).

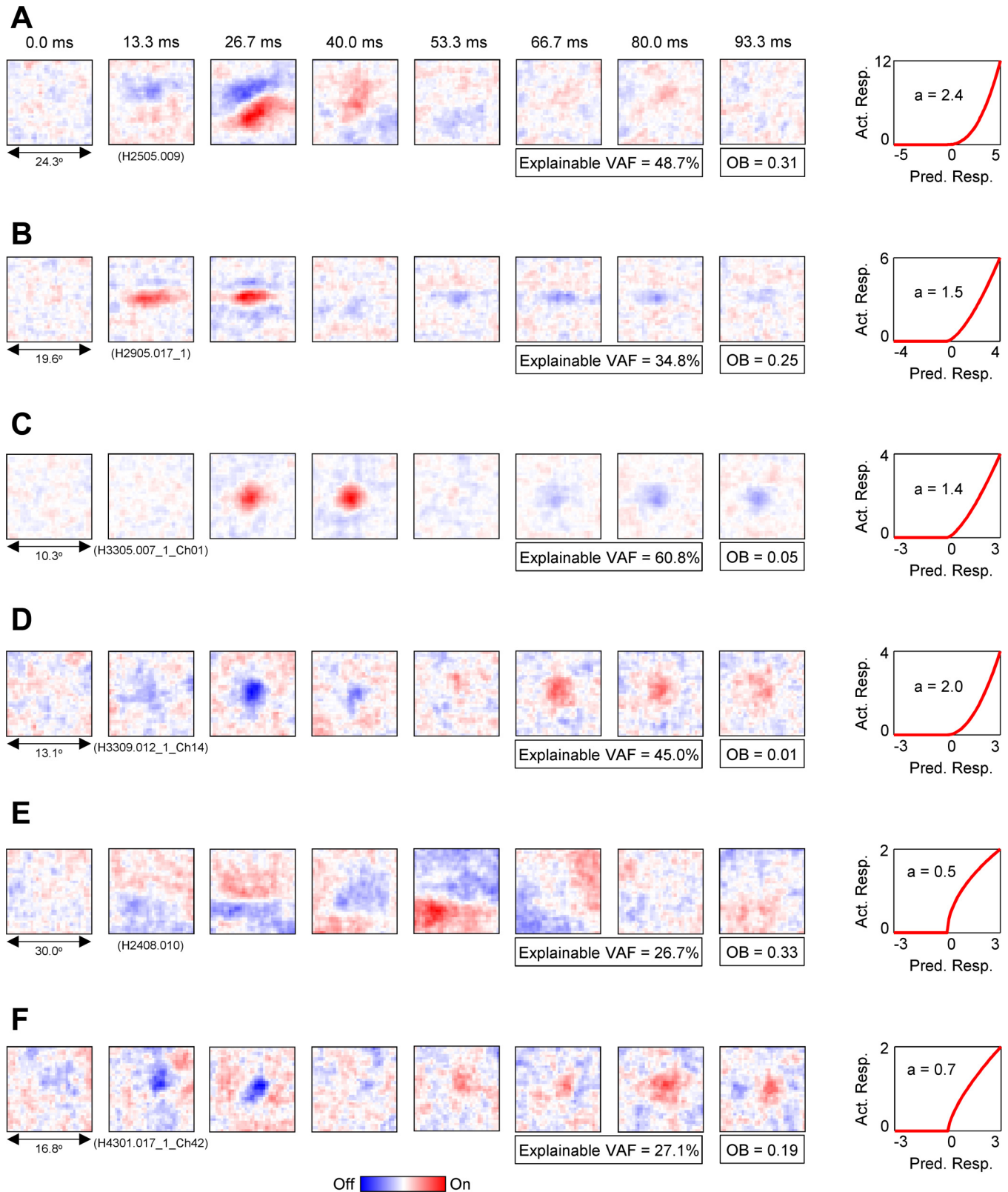
**Three categorical types of RF models.** From inspection of many RF models such as those above, we were most surprised by the wide variation in their orientation selectivity and in their ZMN power, suggesting that the neurons might be categorized in terms of these properties. To quantitatively examine this hypothesis, the OB and ZMN values for the entire sample of simple cells are shown in Fig. 6. A histogram of OB values (Fig. 6A) has a broad range and includes many nonoriented cells with OB < 0.1 as well as oriented cells with larger OB values. The distribution appears bimodal, which is confirmed formally ( $P = 0.03$ ). In Fig. 6B, a histogram of ZMN power values has many neurons with expansive values ( $a = 1.5$ – $2.5$ ) but also has numerous compressive values ( $a < 1.0$ , as low as 0.2). Furthermore, the ZMN power values also exhibit a significantly bimodal distribution ( $P = 0.03$ ). Of all the metrics describing the RF models and spiking behavior examined here, these were the only two that exhibited bimodal distributions that were statistically significant.

In a scatterplot of the ZMN power exponents against the OB values (Fig. 6C), the neurons appear to be grouped into three distinct clusters. To objectively verify the number and distinctness of these apparent clusters, a GMM clustering algorithm (McLachlan and Basford 1988) (see METHODS) was performed on the OB and ZMN power exponent values of our sample. GMM models with varying numbers of clusters ( $N_C$ ) ranging from 1 to 4 were compared using AIC and BIC (Akaike 1974, 1998) (see METHODS). The lowest AIC and BIC values were obtained with a GMM with  $N_C = 3$ , objectively confirming the optimal number of clusters to be three.

These three distinct categories of simple cells revealed by the GMM clustering analysis are illustrated in Fig. 6D as

dashed line ellipses indicating contours at two standard deviations from the cluster centers. These categories will be referred to as nonoriented (nonOri) cells, expansive oriented (expOri) cells, and compressive oriented (compOri) cells. The compOri cells dominate lower ZMN power values, while the

nonOri and expOri cells have higher, overlapping ZMN power values but distinct ranges of orientation bias. Note that the apparent delineation of our three categories (Fig. 6D) appears implausibly sharp, i.e., there are almost no “intermediate” cases—however, it must be remembered that the GMM is a



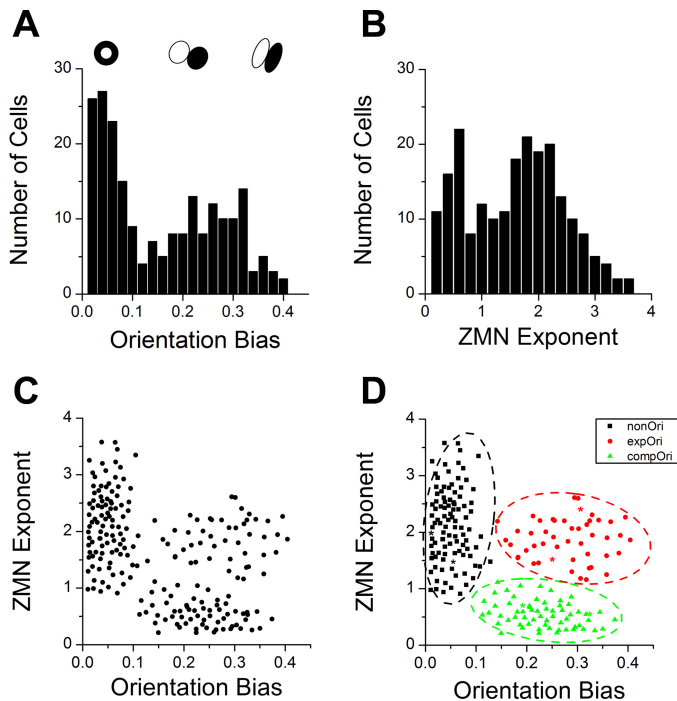


Fig. 6. Orientation bias and output power law exponent values for simple cells. *A*: histogram of orientation bias (OB) values, showing a bimodal distribution. Cartoon RFs reflect degree of oriented RF structure corresponding to OB values. *B*: histogram of nonlinear power exponent ( $a$ ) values, also showing a clear bimodal distribution. *C*: nonlinear power plotted against OB, with each data point representing a single neuron, showing apparent clustering into 3 distinct groups. *D*: scatterplot as in *C*, with existence of 3 distinct groups objectively verified by Gaussian Mixture Model (GMM) clustering. Dotted line ellipses indicate fitted Gaussian distributions for each cluster at 2 standard deviations from cluster centers. The 3 categories are referred to as nonoriented (nonOri) cells, expansive oriented (expOri) cells, and compressive oriented (compOri) cells. Data points depicted by asterisks indicate 6 example cells shown in Fig. 5.

probabilistic model, such that the dashed ellipses in Fig. 6*D* are only indicative of the probabilities of neurons within them belonging to the corresponding cluster.

It is conceivable that our measure of orientation bias might be subject to spurious bimodality (Mechler and Ringach 2002) because of its functional form. Therefore we also analyzed the orientation dependence by finding the best-fitting von Mises function (Eq. 3), which is commonly used to describe circular data (Batschelet 1981; Swindale 1998). A scatterplot like that of Fig. 6*C*, but using the width parameter  $w$  of the best-fitting von Mises function for each neuron, also revealed the same three clusters. A GMM clustering analysis again indicated three clusters as optimal, based on AIC and BIC.

Our analysis has utilized only responses from neurons classified as simple-type cells, but there is evidence that visual cortex neurons may actually lie on a continuum of simplelike to complexlike response properties, varying in the relative contributions of linear and nonlinear response components (Chance et al. 1999; Fournier et al. 2011; Priebe et al. 2004). This idea raises the possibility that some cells in our sample might be relatively more complexlike than others, and thereby provide differing results in our analysis, which only reveals the quasi-linear component. For example, the compOri cells might be somewhat complexlike on such a continuum, with our analysis only revealing the residual linear component. To address this possibility we utilized the responses to optimal or near-optimal drifting sine wave gratings, which were available for 184 of the 212 neurons in our sample. This was frequently possible because our penetrations were approximately orthogonal to the cortical surface, and therefore aligned with the columnar organization for grating tuning properties. We measured the ratio of modulated to unmodulated discharge (AC-DC ratio), which classically gives values greater than unity for simple-type cells (Skottun et al. 1991). The distribution of these values was much like that expected for simple-type cells, with most values between 1.0 and 2.0. The distributions for each type were not evidently different, and none of them was significantly bimodal (Hartigan dip test). Scatterplots of the AC-DC ratios against orientation bias or the exponent of the fitted output nonlinearity (Fig. 7, *B* and *C*) did not reveal any apparent clusters, and the average AC-DC ratios for the three types (Fig. 7*A*) were not statistically significantly different from one another. Consequently, it appears that our three categories do not exhibit any systematic relationship to simplelike vs. complexlike behavior.

A possible inadequacy of our model architecture is the very simplified output nonlinearity function, which was technically advantageous because it has only one free parameter. It might be that the compOri cells are actually similar to the expOri cells, but have negative thresholds, and the half-wave rectification in our function clips relevant inputs below zero—see, for example, Bonin et al. (2006). Another such possibility is that there might be an offset  $y_0$  to the output, notwithstanding our having initially subtracted out the spontaneous activity. In general, variations in either of these offset values might affect our estimates of power law exponents (Mechler and Ringach 2002). To evaluate these ideas, we refit the relationship between measured responses vs. responses predicted by the estimated linear filter (STRF), as described in METHODS, with a rectified power law having an input offset,  $T$ , and also an output offset,  $y_0$ , as additional free parameters:

Fig. 5. Example RF models. *A–F*: examples of estimated space-time receptive field models for 6 neurons. Each panel depicts results for 1 neuron, showing spatiotemporal receptive fields (STRFs) across 8 time lags (0.0 ms to 93.3 ms) and estimated output nonlinearity (half-power law). *A*: a STRF with adjacent, right oblique ON and OFF regions resembling a Gabor-like structure. The cell has strong orientation selectivity, with an OB of 0.31 as well as a zero-memory nonlinearity that is expansive (power exponent  $a = 2.4$ ), and raw/explainable variance accounted for (VAF) of 26.4% and 48.7%, respectively. *B*: a STRF with a horizontally oriented ON region and flanking crescent-shaped OFF lobes. The cell has a weak phase reversal and slight progression of spatial phase across time lags as well as exhibiting strong orientation selectivity, with an OB of 0.25, an expansive output nonlinearity (power exponent 1.5), and raw/explainable VAFs of 25.3% and 34.8%. *C*: a STRF with ON-center, concentric OFF-surround structure and a clear phase reversal at later time lags. The cell shows negligible orientation selectivity, with an OB of 0.05, an expansive nonlinearity with a power of 1.4, and raw/explainable VAFs of 40.9% and 60.8%. *D*: a somewhat noisier OFF-center, ON-surround STRF with a strong phase reversal at later time lags. This cell shows no orientation selectivity, with an OB of 0.01, an expansive nonlinearity with a power of 2.0, and raw/explainable VAFs of 25.1% and 45.0%. *E*: a STRF that is orientation selective, with an orientation bias (OB) of 0.33, a compressive nonlinearity of 0.5, and raw/explainable VAFs of 16.1% and 26.7%. *F*: a STRF with a somewhat nondescript spatial structure. The cell is weakly orientation selective, with an OB of 0.19, a compressive nonlinearity power exponent of 0.7, and raw/explainable VAFs of 14.7% and 27.1%.

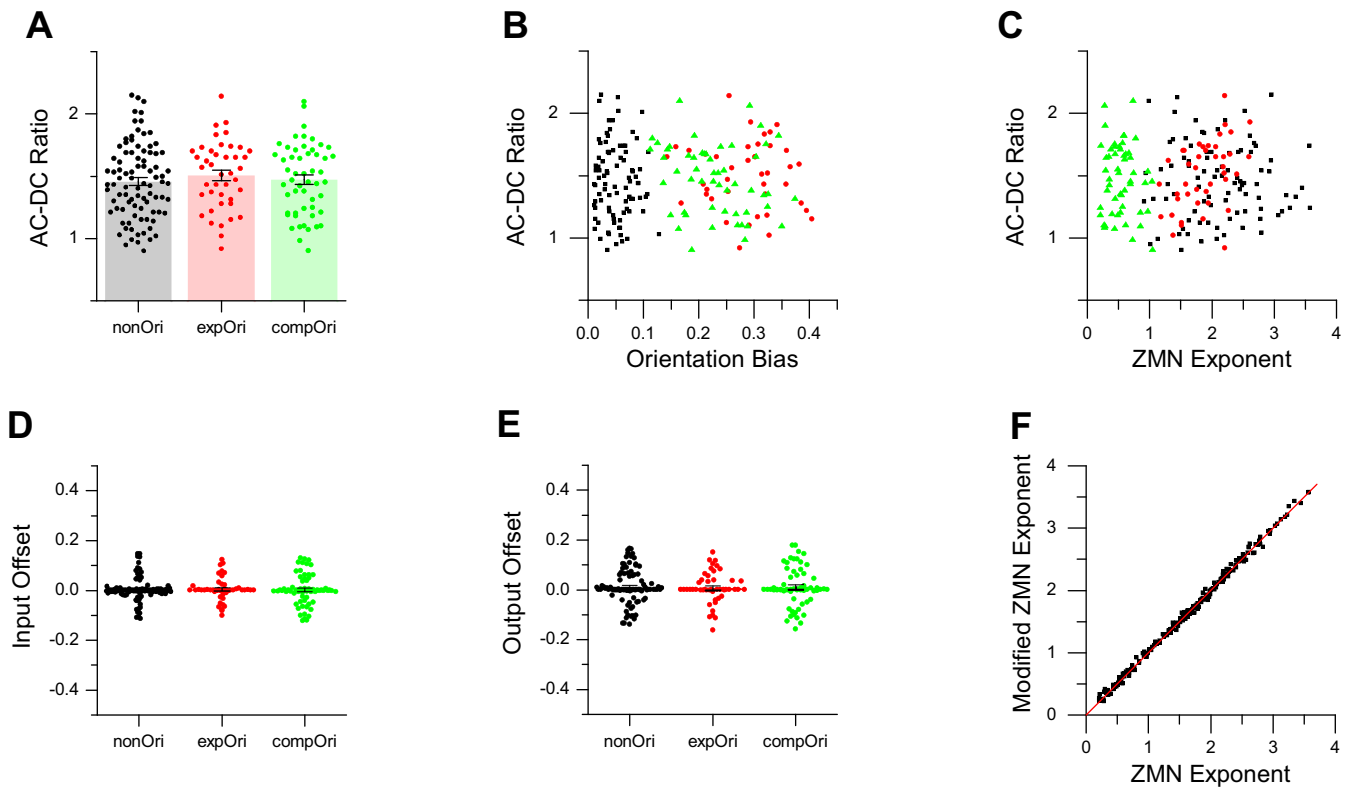


Fig. 7. Relationship of receptive field properties to degree of simplelike vs. complexlike behavior and possible role of offsets in fitted output nonlinearity. *A*: bar chart of mean and SE values for the 3 categories, with superimposed points representing measurements from individual neurons. *B* and *C*: scatterplots of AC-DC ratio vs. orientation bias and nonlinear power exponent values. *D* and *E*: bar charts with superimposed points for input and offset parameters in fits of Eq. 13 to output nonlinearity estimation data. *F*: scatterplot of output nonlinearity exponents estimated from Eq. 13, against values measured with the simpler half-power model without input or offset parameters. Red line indicates 1:1 relationship.

$$y = y_0 + [L(x) - T]^n \quad (13)$$

The fitted values of input offset  $T$  had mean  $\pm$  SE values of  $-0.00231 \pm 0.00466$  for nonOri cells,  $0.00336 \pm 0.00666$  for expOri cells, and  $0.00198 \pm 0.00777$  for compOri cells (Fig. 7*D*). The mean values of  $T$  were not significantly different between any of the three cell types. For each of the three types, the mean  $T$  values were not significantly different from zero. The fitted values of output offset  $y_0$  had mean  $\pm$  SE values of  $0.01046 \pm 0.00662$  for nonOri cells,  $0.00776 \pm 0.00897$  for expOri cells, and  $0.00984 \pm 0.00974$  for compOri cells (Fig. 7*E*). The mean values of  $y_0$  were not significantly different between any of the three cell types. Furthermore, the fitted power law exponent values obtained with or without inclusion of the input and offset parameters are highly similar (Fig. 7*F*). Consequently, we retained our use of the fitted power law exponents from the simpler model in which  $T$  and  $y_0$  are zero.

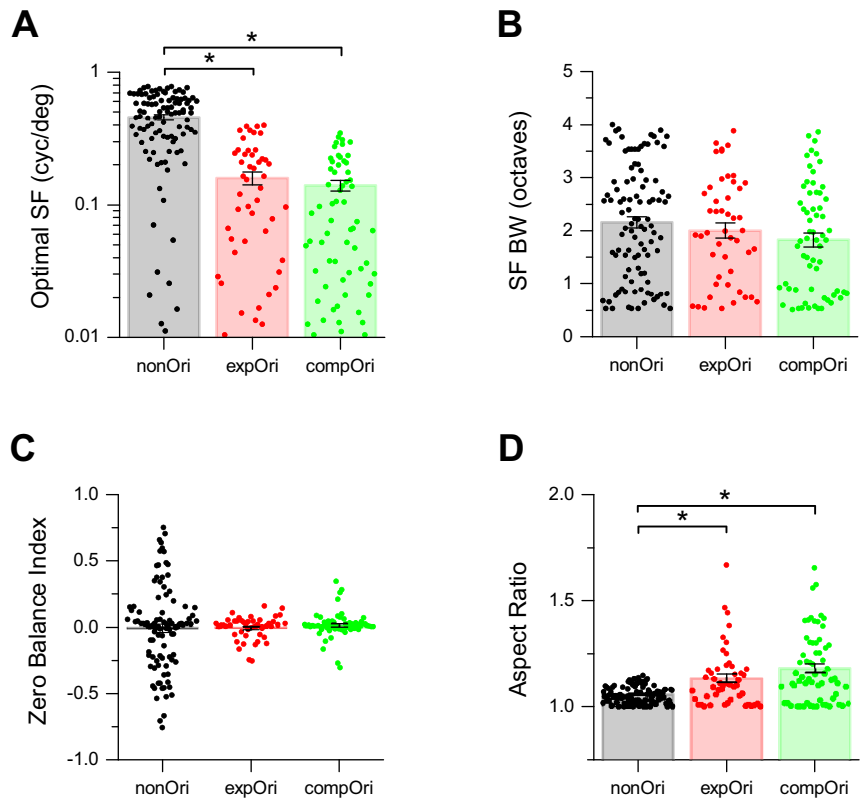
It is conceivable that categorically distinct RF types, particularly expansive vs. compressive output nonlinearities, could be an artifact of spontaneous fluctuations in overall responsivity that are discrete, for example, up and down states (Wilson and Kawaguchi 1996). However, up/down states are short, with transitions occurring in fractions of a second, while the recordings performed here are on the order of an hour. Each recording would therefore contain many hundreds of up/down transitions, and their effects would be averaged out. Therefore it seems highly unlikely that our distinct RF categories could be artifacts of such rapid state fluctuations. There might also be slow changes, for example, due to shifts in depth of anesthesia,

which could alter the percentage of time that the cortex is in desynchronized or synchronized states having different levels of responsivity to stimuli (Harris and Thiele 2011). However, such changes would not be correlated with the times of our data acquisition runs, so that any given run would have a random mix of the two states, thus making a bimodal population distribution unlikely. In addition, we observed a number of instances in which neurons exhibiting both expansive and compressive output nonlinearities were simultaneously recorded on the same multielectrode penetration, sometimes even at the same recording site. Thus in general it seems very unlikely that our categorical separation of cell types is an artifact of fluctuations in brain state.

Although these simple cell categories were distinct based on their orientation bias and output nonlinearity, we also examined other possible dimensions across which these neurons might show distinct responses.

*Spatial response properties.* The estimated RFs varied widely in size, as can be seen in the examples of Fig. 5 (note scale bars, *bottom left*). To quantitatively analyze this variation in spatial scale, we extracted the optimal SF from each RF map at peak latency, as described in METHODS (Eq. 3). Average values of optimal SF of the three categories of simple cells are shown in the bar chart of Fig. 8*A*. The distributions of the values can be visualized from the superimposed points on each bar, which indicate values from individual neurons. Overall these values for the oriented types ( $0.16 \pm 0.02$  cycles/ $^\circ$  for expOri and  $0.14 \pm 0.01$  cycles/ $^\circ$  for compOri) conform

Fig. 8. Spatial receptive field properties for the 3 types of simple cells, shown as bar charts with superimposed symbols depicting values from individual neurons. *A*: optimal spatial frequencies obtained from the analysis shown in Fig. 2. Average optimal SF is significantly higher for nonOri than for expOri or compOri cells. *B*: SF bandwidths obtained from the analysis shown in Fig. 2. Average SF bandwidths (octaves) are not significantly different for the 3 cell types. *C*: zero balance index (ZBI), with values that are negative, zero, or positive representing OFF-dominated, zero-balanced, and ON-dominated RFs. ZBI values for the 3 cell categories all have average values near 0. *D*: aspect ratios estimated by the method shown in Fig. 3. In this and subsequent figures, data points represent measurements from individual neurons, bars indicate means, and error bars indicate SE values, with results for nonOri cells in black, expOri in red, and compOri in green.



broadly to those in the literature for oriented cells in cat A18 (Mareschal and Baker 1998; Movshon et al. 1978; Song and Baker 2006). However, the nonOri cells have a substantially higher average optimal SF ( $0.46 \pm 0.02$  cycles/°), which is significantly larger than for expOri ( $P = 6.8 \times 10^{-16}$ ) and for compOri ( $P = 7.2 \times 10^{-25}$ ).

We wondered whether SF bandwidth contributed in any way to our categorical distinctions in a manner similar to that of orientation bias. One might expect nonOri cells, which have spatial RF structures resembling those found in lateral geniculate nucleus (LGN), to be more broadly tuned for SF than expOri cells with their Gabor-like spatial structure. In addition, the varied spatial RF structures of the compOri cells might give them a broader range of SF bandwidths. However, the measured SF bandwidth values (see METHODS, Eq. 3), shown in Fig. 8B, do not uphold these expectations—the average SF bandwidths are not significantly different across the three categories ( $2.2 \pm 0.11$  octaves for nonOri,  $2.0 \pm 0.14$  for expOri, and  $1.8 \pm 0.13$  for compOri), in each case being broadly distributed across a range from ~0.5 to 4 octaves, in broad agreement with values in the literature for cat A18 (Mareschal and Baker 1998; Movshon et al. 1978).

A RF property that might be related to SF bandwidth is the relative strength of ON and OFF regions in the STRF—in a linear model, an imbalance would enhance responses at low SFs. Also, one might expect nonOri cells to be unbalanced if they are LGN like (i.e., LGN cells often have surrounds weaker than centers), while Gabor-like expOri cells would be roughly balanced. ON/OFF dominance was quantified with the ZBI, described in Eq. 4 in METHODS. A ZBI with a value of 0 signifies balanced ON and OFF zones, while positive or negative values represent ON-dominated or OFF-dominated RF estimates, respectively. The means and distributions of ZBI values for the

three cell categories are shown in Fig. 8C. As expected, the majority of both oriented types are tightly clustered around 0 (expOri =  $-0.0054 \pm 0.013$ , compOri =  $0.015 \pm 0.012$ ), indicating that the majority of these RFs are roughly balanced. The latter result suggests that the wide range of SF bandwidths for the oriented types (Fig. 8B) was not due to variation in ON/OFF imbalance. The ZBI values for nonOri cells, however, reveal a wide range of degrees of ON/OFF imbalance, although the average ( $-0.0087 \pm 0.032$ ) is close to 0.

Another spatial RF property of potential relevance is aspect ratio, i.e., length to width, in relation to the preferred orientation. Conceivably, expOri and compOri cells could have a range of aspect ratios, while nonOri cells should have values of about unity. Measured aspect ratios, calculated from variance maps with the procedure described in METHODS (Eqs 6–9), are shown for the three cell types in Fig. 8D. The average aspect ratios are indeed very close to unity for the nonOri cells ( $1.059 \pm 0.00414$ ), with very little scatter. The expOri cells have higher aspect ratios ( $1.13 \pm 0.0202$ ) that are significantly greater than the nonOri cells ( $P = 2.2 \times 10^{-6}$ ), and the compOri cells are also have higher values ( $1.18 \pm 0.0207$ ) that are significantly greater ( $P = 3.6 \times 10^{-11}$ ). The oriented types show substantial variation among individual neurons, consistent with previous reverse correlation results (Jones and Palmer 1987; Ringach 2002).

*Temporal and spatiotemporal response properties.* A similar approach of using spectra of space-time RF maps to estimate temporal frequency response properties was not employed, since temporal response properties of visual cortical neurons are quite nonlinear (Dean and Tolhurst 1986). Instead, we investigated time-domain properties of response latency (time to peak response) and duration using temporal profiles of space-averaged variance maps (Fig. 3, A and B).

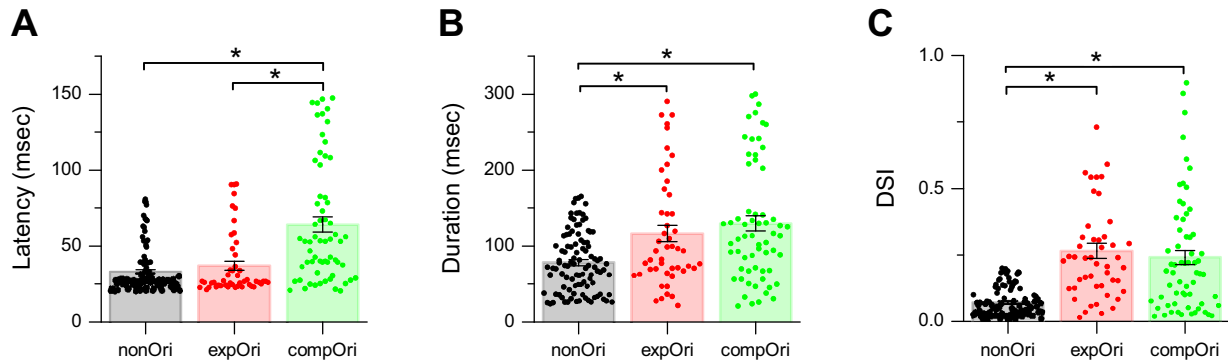


Fig. 9. Temporal and spatiotemporal receptive field properties. *A*: response latency to peak of spatiotemporal receptive field estimated as shown in Fig. 3. Average response latencies are significantly higher for compOri cells than for nonOri or expOri cells. *B*: response duration estimated as shown in Fig. 3. Average response duration is significantly shorter for nonOri cells than for expOri or compOri cells. *C*: direction selectivity index (DSI) values, estimated as shown in Fig. 4, giving index values ranging between 0 and 1, with 0 representing no direction selectivity and 1 representing perfect direction selectivity. Average values for nonOri cells are very small, while those for expOri and compOri are more scattered and significantly larger. \* $P < 0.05$ .

Because of the spatial structure of the nonOri cells, one might expect them to be more directly LGN driven, and therefore likely to have shorter latencies. The results (Fig. 9*A*) show that nonOri and expOri cells have similar, relatively low latencies (population averages of  $32.8 \pm 1.5$  ms and  $36.9 \pm 3.0$  ms, respectively). All three distributions are quite skewed, with the values for compOri cells spread across a particularly wide range of 25–150 ms, with a higher average ( $64.1 \pm 5.0$  ms) that is significantly different from that of the other two types ( $P = 3.1 \times 10^{-11}$  with nonOri,  $3.4 \times 10^{-5}$  with expOri). The average latency (including all 3 of our classes) is 44.6 ms, which is congruent with the average value of 40 ms reported for A18 by Dinse and Kruger (1994).

Some of the STRF maps were distributed across several temporal lags, e.g., Fig. 5*C*, while others were more sharply confined to a few lags, as in Fig. 5*A*. We quantified this property as response duration, estimated as the time between the  $1/e$  of peak temporal envelope values in temporal profiles of variance maps (see METHODS). Similar to response latency, one might expect that if nonOri cells were LGN like, they might have faster temporal dynamics and therefore shorter response durations. The results (Fig. 9*B*) revealed that most nonOri cells have durations ranging from 25 to 150 ms ( $78.1 \pm 3.9$  ms), while the two oriented types additionally included values up to 300 ms. The expOri and compOri cells have roughly equal average durations ( $116 \pm 10.6$  ms and  $130 \pm 9.9$  ms, respectively), in each case significantly greater than the nonOri cells ( $P = 5.8 \times 10^{-5}$  with expOri,  $P = 9.3 \times 10^{-8}$  with compOri). The average duration, including all three types, is 108 ms, which is substantially smaller than the value of 284 ms found for cat A18 neurons by Dinse and Kruger (1994). This difference might have been due to the latter authors' estimation of temporal dynamics from simple step responses.

A direction selectivity index (DSI) was used to quantify space-time nonseparability underlying direction selectivity, as described in METHODS (Eq. 11)—its value ranges from zero (separable, no direction selectivity) to unity (maximally nonseparable, perfect direction selectivity). As seen in Fig. 9*C*, the DSI values for nonOri cells are clustered at very low values (mean  $0.073 \pm 0.005$ ), indicative of space-time separability and a lack of direction selectivity, which is not surprising in view of their isotropic RF structure. The expOri and compOri cells, on the other hand, have a much wider range of DSI

values, from near zero to almost unity, indicating highly varying degrees of directionality. The average DSI values for expOri ( $0.26 \pm 0.03$ ) and compOri ( $0.24 \pm 0.03$ ) are significantly greater than for nonOri cells ( $P = 6.6 \times 10^{-16}$  with expOri,  $6.1 \times 10^{-12}$  with compOri).

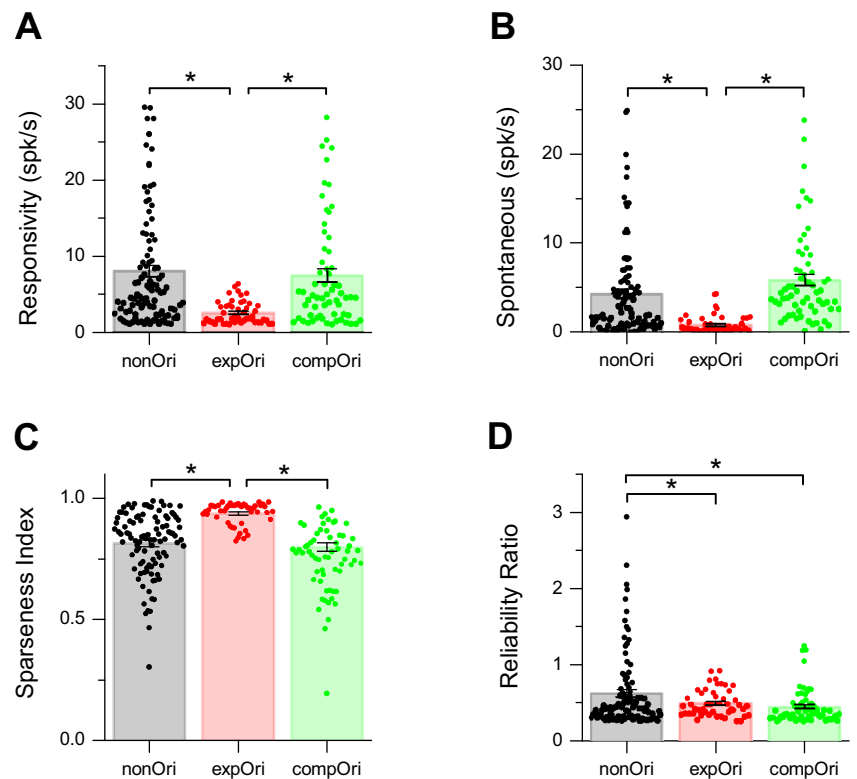
*Spiking response properties and spike waveforms.* In addition to RF properties, visual neurons vary considerably in statistical properties of spiking (Chen et al. 2008; Lesica et al. 2007). Here we examine the extent to which the three cell types might differ in statistical properties of spiking, including both simple measures such as spontaneous activity and responsivity and more complex statistics such as sparseness and reliability.

Measured values of responsivity, quantified as the average spike frequency during NI stimulus presentations (minus the average spontaneous activity), are shown in Fig. 10*A* for the three types. The majority of cells had responsivities ranging from 1 to 10 spk/s, with a minority of the sample having values up to 30 spk/s. One might expect that the lower stimulus selectivity of nonOri cells would result in more vigorous visual responses compared with the other two classes—this expectation is somewhat fulfilled in that the average responsivity for nonOri cells ( $8.03 \pm 0.76$ ) is greater than for expOri cells ( $2.59 \pm 0.21$ ). However, the average compOri responsivity ( $7.46 \pm 0.90$ ) is also similarly greater than for expOri cells. These differences are significant for both nonOri ( $P = 3.0 \times 10^{-6}$ ) and compOri ( $P = 9.3 \times 10^{-6}$ ) types.

The greater responsivity of compOri than expOri cells suggests that the latter operate in the low end of a typical sigmoidal-shaped response function, thereby manifesting an expansive ZMN. The compOri cells respond more vigorously, and so might be operating at the high end of their dynamic range, giving a compressive ZMN. However, there is considerable overlap in the distributions of responsivities, so such a factor could only be a partial explanation.

Spontaneous activity was measured as the average number of spikes during the mean luminance blank screen that preceded each stimulus ensemble. The results for the three types (Fig. 10*B*) again show lower average values for the expOri cells ( $0.83 \pm 0.14$  spk/s) than for the compOri ( $5.80 \pm 0.64$ ) or nonOri ( $4.28 \pm 0.52$ ) cells, with both differences significant ( $P = 1.3 \times 10^{-9}$  and  $P = 1.3 \times 10^{-5}$ , respectively). The distributions of values for the nonOri and compOri cells are

Fig. 10. Spiking response metrics. *A*: average responsiveness are significantly higher for nonOri and compOri cells than for expOri cells. *B*: spontaneous activity (response to blank screen) values are significantly higher for nonOri and compOri than for expOri cells. *C*: lifetime sparseness index (selectivity) values, showing average values significantly higher for expOri than for nonOri and compOri types. *D*: reliability (signal to noise) ratio values, whose average for nonOri is significantly greater than for expOri and compOri cells. \* $P < 0.05$ .



both highly skewed, with a long tail of large values, similar to the responsivity distributions in Fig. 10A.

Sparse coding helps conserve metabolic resources (Laughlin et al. 1998) and is an integral element of theories of efficient coding of NIs (Olshausen and Field 1996; Rehn and Sommer 2007; Vinje and Gallant 2000). We employ an index of lifetime sparseness of spike trains (METHODS, Eq. 12), which ranges from zero (equal response to all stimuli) to unity (response to only 1 stimulus image). Since nonOri cells lack orientation selectivity, one might expect them to have lower sparseness values than the other two types. The results, in Fig. 10C, reveal average values for nonOri ( $0.81 \pm 0.01$ ) that are lower than for expOri ( $0.94 \pm 0.01$ ), by a significant margin ( $P = 2.9 \times 10^{-9}$ ). The compOri cells have an average SI ( $0.80 \pm 0.02$ ) that is also significantly lower than that for expOri ( $P = 3.8 \times 10^{-15}$ ). Sparseness values for the expOri cells are not only greater but also more tightly clustered compared with the wider variation in the other two types.

The trial-to-trial reliability of a neuron's firing to a given stimulus image was measured as a ratio of signal to noise spectral power (Borst and Theunissen 1999), as described in METHODS. As shown in Fig. 10D, the reliability ratios are on average greater for nonOri cells ( $0.62 \pm 0.05$ ) than for either expOri ( $0.49 \pm 0.03$ ) or compOri ( $0.45 \pm 0.03$ ) types, with both differences being significant ( $P = 0.02$  and  $P = 0.01$ , respectively). These values are highly skewed for the nonOri cells, with a long tail of high values.

A different kind of suggested categorical distinction of cortical cells has been between those with thin (narrow) and thick (broad) spike widths, thought to correspond to inhibitory interneurons and excitatory pyramidal cells, respectively (Ami-tai and Connors 1995; McCormick et al. 1985)—however, note that several exceptions to this correspondence have been

demonstrated (e.g., Dykes et al. 1988; Foehring et al. 1991; Gray and McCormick 1996; Kawaguchi and Kubota 1993; Vigneswaran et al. 2011). We employed two measures of spike width (Chen et al. 2008; Frank et al. 2001; Mitchell et al. 2007)—average FWHM of the spike waveform and time from peak to valley. Using either measure, we did not observe significantly bimodal distributions in our sample (Fig. 11, A and B) and so were not able to categorize our neurons on that basis. We also examined the distributions of spike widths for each of our three cell types (Fig. 11, C and D) but found similar distributions and average values that were not significantly different. Thus it is not evident that our three types bear any straightforward relationship to previously reported spike width categories.

*Overview of response properties.* There may well be subtypes within each of our three categories (see DISCUSSION). Several of the distributions in the bar scatter graphs discussed above exhibit substantial scatter, demonstrating an apparent lack of homogeneity, and in some cases seem suggestive of possible bimodal distributions (e.g., compOri in Fig. 9, A and B, nonOri in Fig. 11, C and D). However, none of the indexes formed within-type distributions that had statistically significant bimodality.

Another caveat about our analysis is that it was based on imperfect estimates of RF properties. Our initial assessment of the quality of RF estimates was to measure how much of the response variance of a holdback data set could be predicted (VAF; see METHODS). The estimated RF models here could typically account for  $\sim 15$ – $25\%$  of the response variance, with the population average “raw” VAFs greatest for nonOri cells ( $24.9 \pm 2.1\%$ ), intermediate for expOri ( $20.2 \pm 0.9\%$ ), and lowest for compOri ( $15.1 \pm 1.3\%$ )—these values are in about the same range as found in previous system identification

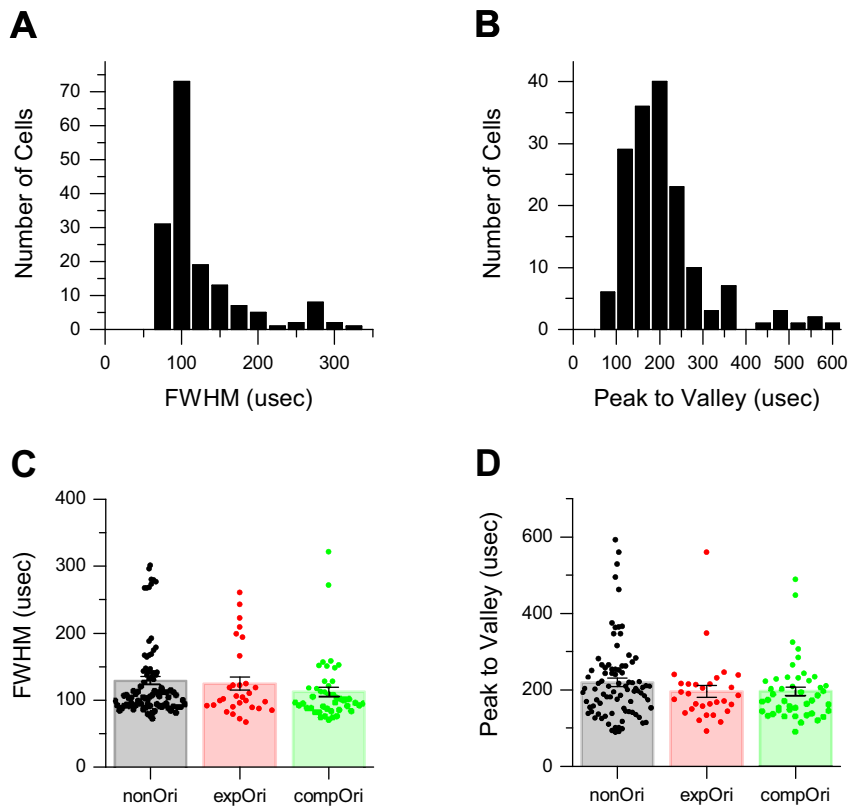


Fig. 11. Spike width measurements. *A*: histogram of widths of sorted spikes, measured as full width at half-maximum (FWHM). *B*: same as *A*, but spike width measured as peak to valley. *C* and *D*: distributions of spike widths for each of the 3 cell types, using the above 2 measures. In either case, the average values were not significantly different.

studies of visual cortex neurons (e.g., David and Gallant 2005; Willmore et al. 2010). However, the amount by which these values are less than 100% can be due both to neuronal response variability (“noise”) and to inadequacies of the assumed LN model architecture. To try to discount the effect of response noise, we used a noise ceiling analysis (METHODS) to obtain an “explainable” VAF—these values (Fig. 12A) are typically ~30–45%. The average explainable VAF for nonOri cells ( $44.6 \pm 2.6\%$ ) was significantly greater than for expOri cells ( $35.4 \pm 1.4\%$ ), which in turn was significantly greater than for compOri cells ( $29.6 \pm 2.6\%$ ). Each of these differences was significant ( $P = 0.04$  and  $P = 0.003$ , respectively).

We wondered why we noted clear distinctions between simple cell types while other research groups have reported a continuum in response properties. An important factor may have been our use of multielectrodes and post hoc spike sorting. Figure 12B shows the numbers of cells in each category isolated with either a window discriminator or post hoc off-line sorting (OFS) with single-channel or multichannel electrodes. Our single-channel recordings with a window discriminator, as used in most previous studies, were heavily biased toward oriented cells (i.e., either expOri or compOri). Single-channel recordings with off-line spike sorting also isolated a much larger fraction of orientation-selective cells. Using multichannel electrodes with off-line sorting, on the other hand, revealed large numbers of nonoriented RFs in addition to the oriented types. These comparisons suggest that the electrode type was not important for finding the two oriented types but that the encounter rate of nonOri cells was much greater for multichannel electrode recordings—this might have been due to electrode sampling characteristics or to

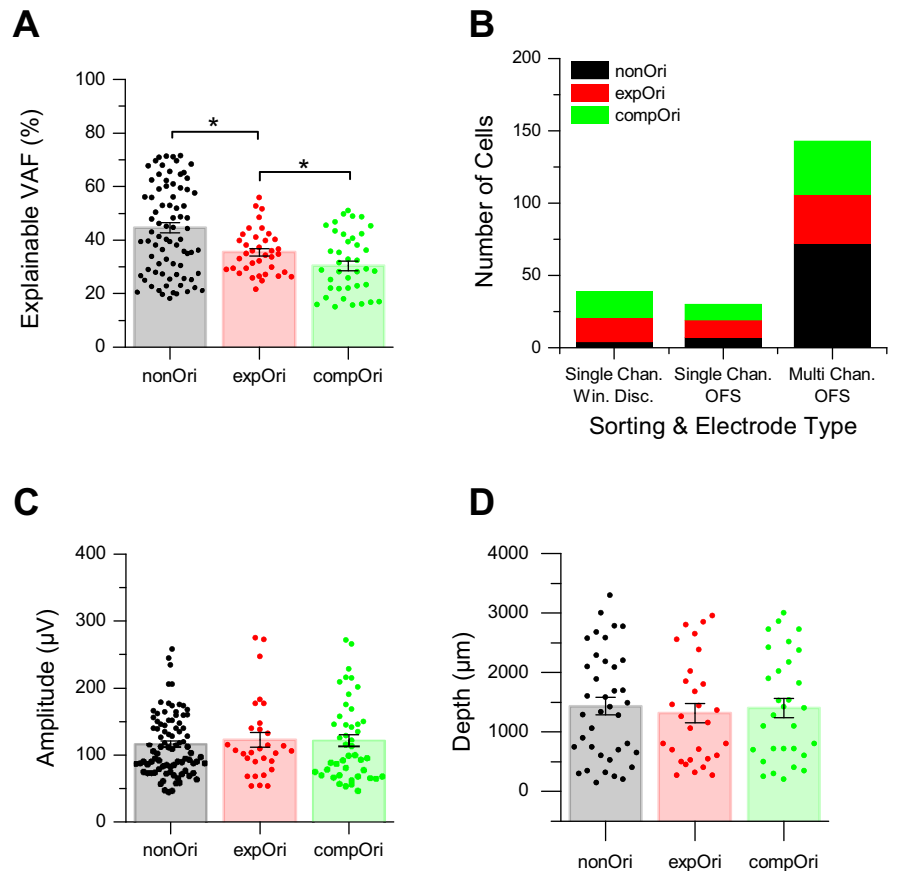
the lack of reliance on a “search stimulus” to look for responsive cells (see DISCUSSION).

Another concern is that many or all of our nonoriented RFs might be measured from thalamic afferents, which have many similarities to the nonOri cells, rather than from cortical neurons. If this were the case, one would expect the measured spike amplitudes to be consistently smaller for the nonOri group than for the other categories. The distributions of spike amplitudes for each of our three categories are shown in Fig. 12C, for the cells that were detected by spike sorting. There is no statistically significant difference in the spike amplitudes for the three types, and the broad dispersions of amplitudes also appear similar.

Thalamic afferent terminals should be seen only within restricted laminae (LeVay and Gilbert 1976), but instead we found them at a wide range of positions (depths) along the linear arrays. Unfortunately, the small pad sizes ( $177 \mu\text{m}^2$ ) of our multielectrodes, chosen for single-unit selectivity, yielded local current source density results that were too noisy to be trustworthy. We instead made approximate estimates of depth based on microdrive readings and the pad spacing of  $100 \mu\text{m}$ , for a subset of the 32-channel linear-array penetrations (Fig. 12D). While this analysis does not provide an accurate laminar localization, it shows that the nonOri cells (as well as the other types) were encountered across the full range of depths, and not localized within limited sets of depths as would be expected if they were thalamic afferents.

While the type of electrode seems to have been important for observing numerous nonoriented RFs, those factors were evidently irrelevant to our finding of distinct expansive vs. compressive output nonlinearity types (expOri and compOri; Fig. 12B). Another important methodological difference from most

Fig. 12. Predictive robustness of receptive field models and distributions with types of recordings. *A*: variance accounted for (VAF) values, indicating ability of receptive field models to predict responses to a holdback validation data set. VAF values range from 0 (no correlation between predicted and measured response) to 100% (perfect prediction). Average explainable VAF values (i.e., incorporating a noise ceiling analysis), shown here, are highest for nonOri cells, intermediate for expOri, and poorest for compOri. *B*: relationship of cell categories to spike sorting method and electrode type. Bar graph illustrates distribution of cell categories using either a window discriminator (Win. Disc.) or post hoc off-line sorting (OFS) with single-channel or multichannel electrodes. Single-channel recordings with a window discriminator are heavily biased toward oriented cells (i.e., either expOri or compOri). Single-channel recordings with OFS also isolated a much larger fraction of orientation-selective cells. Using multichannel electrodes with OFS, however, reveals nearly equal numbers of nonoriented and oriented cell types. *C*: spike waveform amplitudes of sorted units for each of the 3 cell types, which were not significantly different from one another. *D*: distributions of depths at which cells in the 3 categories were encountered, estimated from electrode penetration depths and spacing of recording sites along linear-array multielectrodes. The average depths are not significantly different, but cells from each category are found across the full range of depths. \* $P < 0.05$ .



previous studies was our use of NI stimuli, which can sometimes reveal RF properties not evident when using conventional stimuli (David et al. 2004). To assess whether the type of stimuli might have played a role in the measured output nonlinearities, we compared the ZMN power law exponent values of the estimated RFs for those neurons on which we had also tested more conventional, synthetic stimuli as part of our previous study (Talebi and Baker 2012). Figure 13A shows the power law exponents for neurons on which we also had collected responses to WN as well as NIs. The average values are higher (more expansive) for WN ( $1.89 \pm 0.11$ ) than for NIs ( $1.50 \pm 0.13$ ), and the difference is significant (paired  $t$ -test,  $P = 6.4 \times 10^{-10}$ , d.f. = 44). Examination of the scatterplots reveals that power exponents less than unity (compressive) are seen only for 3 of the 45 WN data sets, with values only slightly below unity (range 0.90–0.94). This difference is illustrated further in histograms of the power law exponents for the two stimuli (Fig. 13, C and E), which are significantly bimodal for NI stimuli ( $P = 0.02$ ) but not for WN. The scatterplot in Fig. 13G shows the relationship between power law exponents measured with WN vs. NIs—the values are highly correlated ( $R = 0.92$ ) but generally higher for noise than for NIs. Note that there is a particularly systematic upward shift for neurons with compressive ( $<1$ ) values for NIs, which acts to erode the bimodal distribution seen with the latter stimuli.

A similar comparison of those neurons on which we also had collected responses to sparse random short bars (SB) shows (Fig. 13B) significantly higher average values (paired  $t$ -test,  $P = 1.2 \times 10^{-10}$ , d.f. = 44) for SB ( $1.89 \pm 0.11$ ) than for NI

( $1.55 \pm 0.12$ ). Again, compressive values are found much more often for the NI responses, with a significantly bimodal distribution for NI (Fig. 13D,  $P = 0.04$ ) but not for SB (Fig. 13F), and only a minority (8 of 45) values (ranging from 0.81 to 0.95). A scatterplot of power law exponents measured with SB vs. NI (Fig. 13F) again shows a high correlation ( $R = 0.95$ ), with a systematic upward shift of small values that prevents bimodality of the distribution.

These results are consistent with previous studies of simple-type cortical cells that found only expansive output nonlinearities with sparse SB (Gardner et al. 1999) or WN (Anzai et al. 1999). Thus it appears likely that our observation of compressive output nonlinearities, and a distinct category of compOri cells, may have been due to our use of NI stimuli.

Our simple cell categories are established on the basis of clear differences in orientation selectivity and output nonlinearity shape (Fig. 6). In addition, the population average values of most of the examined RF and spiking indexes are significantly different across some or all of the cell types—these differences are summarized in Table 1. Also noteworthy are the measures that show no significant relationship with the three cell types: SF bandwidth, ZBI, and spike width.

## DISCUSSION

We have used system identification techniques and NI stimuli to reveal a greater diversity of RF properties in early visual cortex than previously described. Our main finding is that within this diversity we could delineate distinct classes of simple-type cells, based on orientation bandwidth and shape of

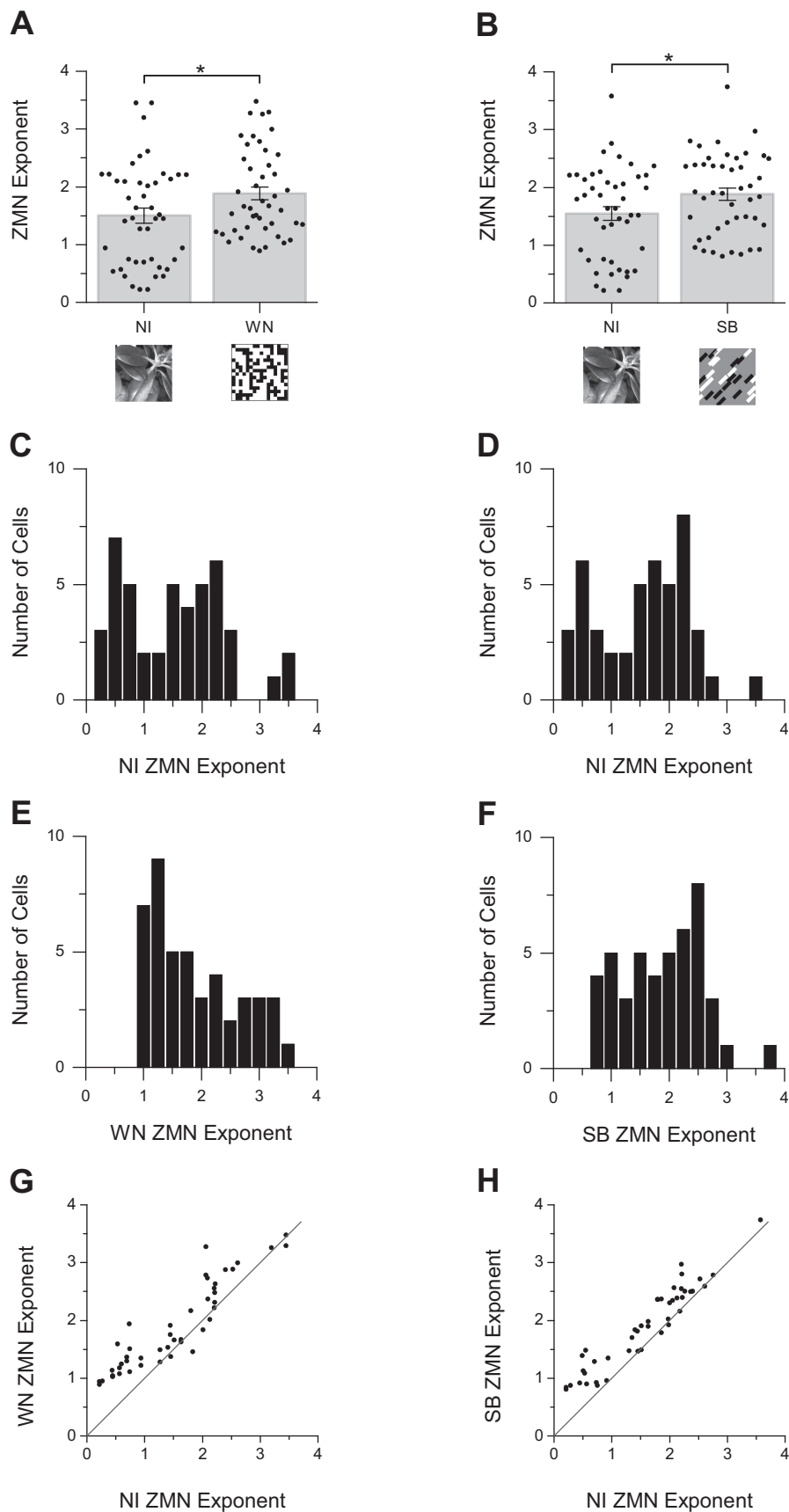


Fig. 13. Measured output nonlinearities for different types of visual stimuli. *A*: values of power law exponents for RF models fit to responses from neurons on which we collected responses to both natural image (NI) and white noise (WN) stimuli. Power law exponents are significantly greater for WN than for NI, with compressive values being frequently seen with NI but rarely with WN. *B*: same comparison for neurons on which sparse short bar (SB) as well as NI responses had been collected. Average power law exponents are significantly smaller for NI than for SB, with the latter again having less tendency to compressive values. *C* and *E*: histograms of power law exponents for NI and WN responses, which are significantly bimodal only for NI. *D* and *F*: same as *C* and *E* for NI and SB responses, which are significantly bimodal only for NI. *G* and *H*: scatterplots of power law exponents obtained from WN (*G*) and SB (*H*) stimuli against exponents measured with NI stimuli—both are highly correlated ( $R = 0.92$  and  $0.95$ , respectively) and show an upward shift for small values that prevents bimodality of distributions for the artificial stimuli.  $*P < 0.05$ .

Table 1. Average differences between the three types of simple cells

	nonOri	expOri	compOri
Optimal SF	Higher	Lower	Lower
Aspect ratio	Lower	Higher	Higher
Latency	Shorter	Shorter	Longer
Duration	Shorter	Longer	Longer
Direction selectivity	None	Mixed	Mixed
Responsivity	Higher	Lower	Higher
Spontaneous	Higher	Lower	Higher
Sparseness	Lower	Higher	Lower
Reliability	Higher	Lower	Lower
VAF	Higher	Intermediate	Lower

output nonlinearity, each of which was relatively numerous. Examples of each of these classes of simple cells have been reported previously but not demonstrated to comprise categorical types. The expOri cells, with an oriented Gabor-like spatial structure and expansive nonlinearity, correspond best to typical previous descriptions of neurons in early visual cortex (e.g., Anzai et al. 1999). The other two categories were seemingly more novel.

**Nonoriented receptive fields.** Orientationally isotropic RFs are well known in primate V1 and have sometimes been reported in cat A17 (e.g., Hirsch et al. 2003; Martinez et al. 2005). An important concern is that our nonOri cells might actually be axonal recordings of thalamic afferent terminals. While we cannot rule out such a possibility based on these findings, it seems unlikely that most of all of our nonOri cells are thalamic afferents, because of their numerosity, their spike amplitudes (Fig. 12C), and the wide range of depths at which they were encountered (Fig. 12D). Axonal recordings would be most likely with high-impedance electrodes such as glass micropipettes, but our highest percentage of nonOri cells was recorded with relatively low-impedance multielectrode arrays (Fig. 12B). In addition, the spike waveforms were not noticeably different from those of the other two types—all were biphasic or triphasic, with the first phase negative-going—characteristic of somatically rather than axonally recorded spikes (Petrusca et al. 2007). Also the nonOri cells' center and surround subfields were on average zero-balanced (Fig. 7C), whereas LGN RFs often have weaker surrounds than centers. Consistent with this, the nonOri cells were band pass in SF, with bandwidths that were similar to those of oriented RFs (Fig. 7B)—in contrast, LGN cells often have broader bandwidths, with very shallow low-frequency rolloffs.

Since our RF estimation employed an LN model architecture, it is conceivable that in these cases we might be fitting a (nonoriented) linear component of complex-type cell responses. However, this was not the case, since the AC-DC ratios of grating responses were almost all greater than unity of nonOri cells (Fig. 7), indicating that they were not complex-type cells. Also, one would then expect the RF models from nonOri cells to be particularly poor at predicting responses, but in fact the nonOri cells exhibited the best prediction VAFs of the three types (Fig. 12A). These VAFs are far too high for what neurons with complex-type RF properties can deliver with this type of quasi-linear model-based analysis.

Why do we observe so many nonoriented RFs, when most previous studies in cat visual cortex did not? This difference is unlikely to be due to our use of NI stimuli, since we also found

very similar nonoriented RFs in response to WN or short oriented bars (Talebi and Baker 2012, Fig. 8). A possible reason for the much greater prevalence of nonoriented RFs might be that in the cat they are much more numerous in A18 than in A17 and that most previous studies of cat visual cortex were in A17. Probably a relevant factor is also our use of multielectrodes, which yielded a much greater percentage of nonOri cells than conventional single-channel electrodes (Fig. 12B) used in previous studies. The multielectrodes may have different recording characteristics, but we suspect the most important consequence may be an associated sampling effect: most of our recordings with multichannel probes used “blind” recording followed by post hoc spike sorting rather than the traditional use of an oriented search stimulus for initial assessment of individual RFs (Koster and Olshausen 2013). The strong surrounds of many of the nonOri cells (Fig. 8C) would diminish their responses to bars or edges, thereby making their visual responsivity more difficult to notice. Indeed, having been alerted to this possibility, we have subsequently been better able to find nonoriented RFs using manual search stimuli, by employing small flashed spots for neurons that seemed unresponsive to bars.

**Compressive output nonlinearities.** Previous quantitative analyses of early cortical simple-type cells using LN models have usually indicated expansive rather than compressive output nonlinearities (Anzai et al. 1999). Compressive output nonlinearities have been reported in a minority of early cortical neurons' responses to gratings (Xing et al. 2011), though not as part of a bimodal distribution of function shapes. In our study compressive output exponents were responses to NI but not to WN or SB stimuli (Fig. 13) that have been used in many of the previous studies. The dependence of the RF model on the stimulus type suggests inadequacy of the model architecture (David et al. 2004) and is consistent with these cells giving the lowest explainable VAFs of our three types (Fig. 12A). A future research direction will be to find ways to estimate more elaborate (nonlinear) model architectures that may better capture these neurons' response properties.

The dependence on stimulus type and the low VAFs might suggest that the compOri cells are relatively more complexlike than those in the other categories, i.e., having both linear and nonlinear response components. If so, then one would expect cells with more compressive output nonlinearities to have lower AC-DC ratios. However, in Fig. 7, the scatterplot of power exponent vs. AC-DC ratio does not show any such systematic relationship—the bar/scatter graph shows that AC-DC ratios were similar for all three cell types.

Fournier et al. (2011) have demonstrated that the type of stimulus can shift a cortical neuron's responses from relatively simplelike to more complexlike behavior. This finding raises the possibility that cortical neuron responses might be simplelike to gratings but more complexlike to NI, perhaps more so for compOri than for expOri cells. Something like this is conceivable, but our results nevertheless indicate categorically distinct types of cells with respect to the degree to which such a shift can occur.

**Categorically distinct cortical receptive fields.** Mechler and Ringach (2002) demonstrated that a simple nonlinear transformation of a unimodal distribution (of values of a RF parameter) could give rise to a bimodal distribution, suggesting that bimodal distributions could result from the manner in which

responses are analyzed rather than reflecting a fundamental distinction. Such a possibility cannot be ruled out entirely for the bimodality of either the orientation bias (OB) measure of orientation selectivity or the power law exponent—in this respect our categorical scheme must remain provisional until further evidence is available. However, an alternative analysis of the orientation dependences using best-fitting von Mises functions also revealed the same clustering. As discussed above, it is entirely conceivable that the compressive output nonlinearities that we observe might result from some other underlying property, but that would not necessarily undermine the idea of these neurons comprising a categorically distinct type.

Several previous neurophysiological studies have considered early cortical neurons in terms of proposed types (e.g., Schiller et al. 1976), but most of these studies did not provide objective evidence, such as bimodal histograms or cluster analyses, that the proposed types were categorically distinct. A notable exception is Willmore et al. (2010), who used NI responses of macaque V2 neurons, analyzed with a wavelet basis transformation, to reveal two major clusters of neurons whose RFs differed in complexity of SF and orientation components and amount of nonlinear suppression. It is tempting to suppose their clusters might be related to ours, although this is difficult to determine since their analysis was substantially different and included complex- as well as simple-type RFs.

We believe that there are two main reasons why these classes of cells have not been previously recognized. The first reason, discussed above, is the combination of multielectrodes and “blind” sampling, which avoids potential difficulties in finding the nonOri cells with conventional manual search stimuli. The second reason is our use of NI stimuli, which reveal many neurons having compressive output nonlinearities when simple artificial stimuli do not (Fig. 13). RF properties, and the delineation of categories, clearly can depend on the stimuli used to measure them. The complex properties of more naturalistic stimuli are likely to provide a richer characterization of RF properties. In the example here, the stimulus dependence of compressive nonlinearities might be due to NI having a broad, continuous range of contrasts, whereas the artificial stimuli have a sharply limited range (binary for dense noise, ternary for sparse bars).

Comparison of orientation bandwidth measurements from previous studies is additionally complicated by the data sets used to measure them. Most previous studies measured responses only at a very limited number of orientation values, as part of a conventional tuning curve measurement. Orientation bandwidth (OB) values from such measurements can be quite different—for example, some neurons may give a good response at only one tested value, thereby giving a very high OB value, while the RF map from such a neuron (e.g., Fig. 2D) will generate some responses at many nonoptimal values and thus give a smaller OB value. It is possible that the limited number of tested orientation values might have prevented observation of a bimodal distribution of OB.

The LN model architecture underpinning our analysis is unquestionably an incomplete description of cortical neurons' RF properties, even for simple-type cells. For example, an LN model does not account for surround modulation (Tanaka and Ohzawa 2009) or second-order processing (Mareschal and Baker 1998). It may nevertheless subsume and at least partially

describe many nonlinear neuronal properties—for example, a compressive nonlinearity would capture some of the effects of contrast gain control. However, it seems unlikely that a more complex model architecture would then reveal a continuum of RF properties—if anything, the errors inherent in an oversimplified (LN) model would tend to obscure categorical distinctions rather than impose or accentuate them.

It is entirely likely that each of our categories may contain multiple subtypes, particularly in view of the known diversity in cellular morphology and molecular features (Brown and Hestrin 2009; Kepecs and Fishell 2014), which presumably evolved to support distinct physiological attributes. Within each category, there is a considerable diversity in other properties (Figs. 7–10), and it may be that a larger sample size could help reveal further divisions.

*Computational functionality.* The prevalence of nonOri and compOri cells might suggest a revision of the standard model of early cortical processing, consisting of a simple bank of Gabor-like filters that are tuned to a series of orientations and spatial frequencies, each having an expansive output nonlinearity to improve selectivity (Albrecht and Geisler 1991; Anzai et al. 1999; Gardner et al. 1999). Computational modeling of optimal overcomplete coding (Olshausen et al. 2009; Rehn and Sommer 2007) suggests that a wider variety of filter shapes may be necessary to provide an adequate “basis set” for representation of natural images. From this point of view it would be especially interesting to examine whether similar such RF types occur in primary visual cortex (A17/V1).

A compressive output nonlinearity would seem undesirable, since it would degrade selectivity—however, this may simply reflect a greater engagement of a divisive gain control (Carandini and Heeger 2012), which would retain rather than degrade the filter selectivity. This idea is consistent with compOri cells having greater responsivity (Fig. 10A) and a stronger degree of nonlinearity as indicated by their lower VAFs (Fig. 12A).

The three RF types might embody a hierarchical progression of more elaborated RF properties with increasing feature selectivity, from the nonOri to expOri to compOri type. The nonOri cells are similar to LGN cells not only in their orientational isotropy but also in their small RF sizes (Fig. 8A) and lack of direction selectivity (Fig. 9C), but unlike LGN cells nonOri cells often have balanced RFs (Fig. 8C), giving them SF bandwidths similar to oriented RFs (Fig. 8B). Taken together, these results are consistent with the idea that these cells could act as an intermediate processing stage between LGN afferents and cells with oriented RFs, for example, to provide push-pull inputs that are contrast invariant (Troyer et al. 1998). In general, nonoriented concentric RFs have surrounds that increase in strength moving from the retina to the LGN and then to cortex, exemplifying a progressive refinement of RF properties with higher levels of processing. Also consistent with a hierarchy is the progressive increase of nonlinearity, as reflected in VAFs (Fig. 12A), from nonOri to expOri to compOri type, which might reflect more elaborate RF properties.

Compressive output nonlinearities have been proposed as components of more complex nonlinear models of extrastriate cortical processing (Kay et al. 2013; Mineault et al. 2012; Nishimoto and Gallant 2011), in which they occur at an intermediate stage prior to summation of an earlier layer of filters. In that regard, compOri cells might function as early

subunits for later-stage neurons, in the same or a higher brain area. For example, a higher-level neuron might compute an approximation to a multiplicative interaction or AND-gating by compressive summation of early-stage neurons and a final expansive nonlinearity (Gabbiani et al. 2004; Mineault et al. 2012).

**Future directions.** It will be important to examine whether similar categories are found in primary visual cortex (A17) of the cat, where most previous studies did not observe so many nonoriented cells or compressive output nonlinearities—it is conceivable that these properties might be unique to A18. Also, it will be of much interest to conduct similar studies in primate visual cortex, both V1 and V2.

Our categories are probably not homogeneous—i.e., we anticipate that there may be subtypes within them. It may be possible to delineate categorically distinct subtypes of visual cortex cells by utilizing more elaborate model architectures that can better capture additional nonlinear phenomena of cortical neurons, such as divisive normalization (Carandini and Heeger 2012), and by establishing relationships to cell types defined by morphology, molecular markers, or intracellular electrophysiological properties. In addition, it would be desirable to include complex-type cells, which are not amenable to the type of analysis used here—use of a different kind of model architecture and analysis that could be applied uniformly to cells having both simple and complex RF properties (e.g., see Fournier et al. 2011) might reveal a more complete characterization of discrete types of neurons.

With the increasing use of multineuron recording methods, traditional tuning curve characterizations conducted in a manner specific to each neuron are often not viable, making system identification approaches using complex stimuli more attractive. This trend will have the benefit of helping avoid sampling biases from the use of manual search stimuli, instead using indiscriminate recording from many neurons simultaneously. More natural stimuli might be particularly useful in this context, especially for delineation of RF types. Different RF categories presumably have distinct functional roles, e.g., signaling different portions of the stimulus space, which could be most effectively revealed by using naturalistic stimuli. Our stimuli used here contained spatial images from natural scenes, but they were presented without temporal correlation. An important future improvement would be to employ stimuli that are more fully “natural,” for example, to use image sequences that simulate normally occurring eye movements (Baudot et al. 2013).

Laminar organization of these physiological cell types might be expected since neuronal properties are known to vary across laminae (e.g., Martinez et al. 2005; Murthy et al. 1998). Morphologically defined cell types often occur in specific laminae, and different cortical layers receive distinct inputs from other brain areas as well as projecting to distinct targets. In this study we did not have sufficient information for laminar localization but noted a dispersion of the three cell types across depths. Nevertheless, a useful future research direction might be laminar localization of these RF types, for example, with current source density analysis (Mitzdorf 1985; Pettersen et al. 2006). This effort might be especially worthwhile in species such as macaque monkeys, which have more pronounced laminar differentiation than observed in the cat.

**Conclusions.** Much of our understanding of the nervous system’s functional circuitry has been built upon a framework of neuronal taxonomy—physiologically defined cell types corresponding to distinct anatomical characteristics, for example, in the retina (Masland 2012) or superior colliculus (Gale and Murphy 2014). The mammalian visual cortex contains dozens of neuronal cell types defined by morphology (Brown and Hestrin 2009), responses to intracellularly injected current (Nowak et al. 2003), or expression of specific markers (Kepecs and Fishell 2014), but the functional roles of these cell types in processing visual information are poorly understood. Lund and Wu (1997) described nearly 40 morphologically distinct subtypes of interneurons (e.g., chandelier, neurogliaform, basket cells), and recently there has been notable progress toward establishing correspondence of these types with physiological roles (e.g., Adesnik et al. 2012; Kepecs and Fishell 2014). It will be of great interest to explore whether the above cell types bear a correspondence to RF types such as those described here.

In conclusion, our findings indicate discrete, physiologically defined types of cortical RFs that may have distinct functional roles and connections. Establishing a full physiological taxonomy of types of neurons may be critically important to provide a more well-defined framework upon which to build an incisive understanding of cortical circuitry and function, and to construct more meaningful computational models of visual signal processing.

#### ACKNOWLEDGMENTS

The authors thank Michael Oliver of the J. Gallant lab at University of California-Berkeley for generously providing regression analysis software and useful advice. We also thank Linda Domazet, Amol Gharat, Guangxing Li, Zhengchun Wang, Zhimo Yao, and Nini Yuan for assistance with experiments. We are grateful to Guangxing Li for contributions to software and for comments on the manuscript.

#### GRANTS

This work was supported by Canadian Institutes of Health Research Grants MA-9685 and MOP-119498.

#### DISCLOSURES

No conflicts of interest, financial or otherwise, are declared by the author(s).

#### AUTHOR CONTRIBUTIONS

V.T. and C.L.B. conception and design of research; V.T. performed experiments; V.T. analyzed data; V.T. and C.L.B. interpreted results of experiments; V.T. prepared figures; V.T. drafted manuscript; V.T. and C.L.B. approved final version of manuscript; C.L.B. edited and revised manuscript.

#### REFERENCES

- Adesnik H, Bruns W, Taniguchi H, Huang ZJ, Scanziani M. A neural circuit for spatial summation in visual cortex. *Nature* 490: 226–231, 2012.
- Akaike H. A new look at the statistical model identification. *IEEE Trans Automat Contr* 19: 716–723, 1974.
- Akaike H. A Bayesian analysis of the minimum AIC procedure. In: *Selected Papers of Hirotugu Akaike*, edited by Parzen E, Tanabe K, Kitagawa G. New York: Springer, 1998, p. 275–280.
- Albrecht DG, Geisler WS. Motion selectivity and the contrast-response function of simple cells in the visual cortex. *Vis Neurosci* 7: 531–546, 1991.
- Amitai Y, Connors BW. Intrinsic physiology and morphology of single neurons in neocortex. *Cereb Cortex* 11: 299–331, 1995.

- Anzai A, Ohzawa I, Freeman RD.** Neural mechanisms for processing binocular information I. Simple cells. *J Neurophysiol* 82: 891–908, 1999.
- Baker CL Jr.** Linear filtering and nonlinear interactions in direction-selective visual cortex neurons: a noise correlation analysis. *Vis Neurosci* 18: 465–485, 2001.
- Batschelet E.** *Circular Statistics in Biology*. London: Academic, 1981.
- Baudot P, Levy M, Marre O, Monier C, Pananceau M, Fregnac Y.** Animation of natural scene by virtual eye-movements evokes high precision and low noise in V1 neurons. *Front Neural Circuits* 7: 206, 2013.
- Bonin V, Mante V, Carandini M.** The statistical computation underlying contrast gain control. *J Neurosci* 26: 6346–6353, 2006.
- Borst A, Theunissen FE.** Information theory and neural coding. *Nat Neurosci* 2: 947–957, 1999.
- Brainard DH.** The Psychophysics Toolbox. *Spat Vis* 10: 433–436, 1997.
- Brown SP, Hestrin S.** Cell-type identity: a key to unlocking the function of neocortical circuits. *Curr Opin Neurobiol* 19: 415–421, 2009.
- Carandini M, Heeger DJ.** Normalization as a canonical neural computation. *Nat Rev* 13: 51–62, 2012.
- Chance FS, Nelson S, Abbott LF.** Complex cells as cortically amplified simple cells. *Nat Neurosci* 2: 277–282, 1999.
- Chen Y, Martinez-Conde S, Macknik SL, Bereshpolova Y, Swadlow HA, Alonso JM.** Task difficulty modulates the activity of specific neuronal populations in primary visual cortex. *Nat Neurosci* 11: 974–982, 2008.
- Chklovskii DB.** Synaptic connectivity and neuronal morphology: two sides of the same coin. *Neuron* 43: 609–617, 2004.
- Conway BR, Livingstone MS.** Spatial and temporal properties of cone signals in alert macaque primary visual cortex. *J Neuroscience* 26: 10826–10846, 2006.
- David SV, Gallant JL.** Predicting neuronal responses during natural vision. *Network* 16: 239–260, 2005.
- David SV, Vinje WE, Gallant JL.** Natural stimulus statistics alter the receptive field structure of V1 neurons. *J Neurosci* 24: 6991–7006, 2004.
- Dean AF, Tolhurst DJ.** Factors influencing the temporal phase of response to bar and grating stimuli for simple cells in the cat striate cortex. *Exp Brain Res* 62: 143–151, 1986.
- DeAngelis GC, Freeman RD, Ohzawa I.** Length and width tuning of neurons in the cat's primary visual cortex. *J Neurophysiol* 71: 347–374, 1994.
- DeAngelis GC, Ohzawa I, Freeman RD.** Spatiotemporal organization of simple-cell receptive fields in the cat's striate cortex. II. Linearity of temporal and spatial summation. *J Neurophysiol* 69: 1118–1135, 1993.
- Dinse HR, Kruger K.** The timing of processing along the visual pathway in the cat. *Neuroreport* 5: 893–897, 1994.
- Dragoi V, Turcu CM, Sur M.** Stability of cortical responses and the statistics of natural scenes. *Neuron* 32: 1181–1192, 2001.
- Dykes RW, Lamour Y, Diadori P, Landry P, Dutar P.** Somatosensory cortical neurons with an identifiable electrophysiological signature. *Brain Res* 441: 48–58, 1988.
- Felsen G, Dan Y.** A natural approach to studying vision. *Nat Neurosci* 8: 1643–1646, 2005.
- Felsen G, Touryan J, Han F, Dan Y.** Cortical sensitivity to visual features in natural scenes. *PLoS Biol* 3: e342, 2005.
- Foehring RC, Lorenzon NM, Herron P, Wilson CJ.** Correlation of physiologically and morphologically identified neuronal types in human association cortex in vitro. *J Neurophysiol* 66: 1825–1837, 1991.
- Fournier J, Monier C, Pananceau M, Fregnac Y.** Adaptation of the simple or complex nature of V1 receptive fields to visual statistics. *Nat Neurosci* 14: 1053–1060, 2011.
- Frank LM, Brown EN, Wilson MA.** A comparison of the firing properties of putative excitatory and inhibitory neurons from CA1 and the entorhinal cortex. *J Neurophysiol* 86: 2029–2040, 2001.
- Gabbiani F, Krapp HG, Hatsopoulos N, Mo CH, Koch C, Laurent G.** Multiplication and stimulus invariance in a looming-sensitive neuron. *J Physiol (Paris)* 98: 19–34, 2004.
- Gale SD, Murphy GJ.** Distinct representation and distribution of visual information by specific cell types in mouse superficial superior colliculus. *J Neurosci* 34: 13458–13471, 2014.
- Gardner JL, Anzai A, Ohzawa I, Freeman RD.** Linear and nonlinear contributions to orientation tuning of simple cells in the cat's striate cortex. *Vis Neurosci* 16: 1115–1121, 1999.
- Gray CM, McCormick DA.** Chattering cells: superficial pyramidal neurons contributing to the generation of synchronous oscillations in the visual cortex. *Science* 274: 109–113, 1996.
- Hagiwara K.** Regularization learning, early stopping and biased estimator. *Neurocomputing* 48: 937–955, 2002.
- Harris KD, Thiele A.** Cortical state and attention. *Nat Rev* 12: 509–523, 2011.
- Hartigan JA, Hartigan PM.** The dip test of unimodality. *Ann Stat* 13: 70–84, 1985.
- Heeger DJ.** Half-squaring in responses of cat striate cells. *Vis Neurosci* 9: 427–443, 1992.
- Hegde J, Van Essen DC.** Selectivity for complex shapes in primate visual area V2. *J Neurosci* 20: RC61, 2000.
- Hirsch JA, Martinez LM, Pillai C, Alonso JM, Wang Q, Sommer FT.** Functionally distinct inhibitory neurons at the first stage of visual cortical processing. *Nat Neurosci* 6: 1300–1308, 2003.
- Hubel DH, Wiesel TN.** Receptive fields of single neurones in the cat's striate cortex. *J Physiol* 148: 574–591, 1959.
- Jones JP, Palmer LA.** The two-dimensional spatial structure of simple receptive fields in cat striate cortex. *J Neurophysiol* 58: 1187–1211, 1987.
- Kawaguchi Y, Kubota Y.** Correlation of physiological subgroupings of nonpyramidal cells with parvalbumin- and calbindinD28k-immunoreactive neurons in layer V of rat frontal cortex. *J Neurophysiol* 70: 387–396, 1993.
- Kay K, Winawer J, Mezer A, Wandell BA.** Compressive spatial summation in human visual cortex. *J Neurophysiol* 110: 481–494, 2013.
- Kepecs A, Fishell G.** Interneuron cell types are fit to function. *Nature* 505: 318–326, 2014.
- Kleiner M, Brainard DH, Pelli DG.** What's new in Psychtoolbox-3. *Perception* 36: 1, 2007.
- Koster U, Olshausen B.** *Testing our conceptual understanding of V1 function*. arXiv arXiv: 1311.0778, 2013.
- Laughlin SB, de Ruyter van Steveninck RR, Anderson JC.** The metabolic cost of neural information. *Nat Neurosci* 1: 36–41, 1998.
- Lesica NA, Jin J, Weng C, Yeh CI, Butts DA, Stanley GB, Alonso JM.** Adaptation to stimulus contrast and correlations during natural visual stimulation. *Neuron* 55: 479–491, 2007.
- LeVay S, Gilbert CD.** Laminar patterns of geniculocortical projection in the cat. *Brain Res* 113: 1–19, 1976.
- Leventhal AG, Wang Y, Pu M, Zhou Y, Ma Y.** GABA and its agonists improved visual cortical function in senescent monkeys. *Science* 300: 812–815, 2003.
- Li G, Talebi V, Yoonessi A, Baker CL Jr.** A FPGA real-time model of single and multiple visual cortex neurons. *J Neurosci Methods* 193: 62–66, 2010.
- Lund JS, Wu CQ.** Local circuit neurons of macaque monkey striate cortex. IV. Neurons of laminae 1-3A. *J Comp Neurol* 384: 109–126, 1997.
- Malone BJ, Kumar VR, Ringach DL.** Dynamics of receptive field size in primary visual cortex. *J Neurophysiol* 97: 407–414, 2007.
- Mareschal I, Baker CL Jr.** A cortical locus for the processing of contrast-defined contours. *Nat Neurosci* 1: 150–154, 1998.
- Martinez LM, Wang Q, Reid RC, Pillai C, Alonso JM, Sommer FT, Hirsch JA.** Receptive field structure varies with layer in the primary visual cortex. *Nat Neurosci* 8: 372–379, 2005.
- Masland RH.** The neuronal organization of the retina. *Neuron* 76: 266–280, 2012.
- McCormick DA, Connors BW, Lighthall JW, Prince DA.** Comparative electrophysiology of pyramidal and sparsely spiny stellate neurons of the neocortex. *J Neurophysiol* 54: 782–806, 1985.
- McLachlan GJ, Basford KE.** *Mixture Models: Inference and Applications to Clustering*. New York: Dekker, 1988.
- Mechler F, Ringach DL.** On the classification of simple and complex cells. *Vision Res* 42: 1017–1033, 2002.
- Mineault PJ, Khawaja FA, Butts DA, Pack CC.** Hierarchical processing of complex motion along the primate dorsal visual pathway. *Proc Natl Acad Sci USA* 109: E972–E980, 2012.
- Mitchell JF, Sundberg KA, Reynolds JH.** Differential attention-dependent response modulation across cell classes in macaque visual area V4. *Neuron* 55: 131–141, 2007.
- Mitzdorf U.** Current source-density method and application in cat cerebral cortex: investigation of evoked potentials and EEG phenomena. *Physiol Rev* 65: 37–100, 1985.
- Movshon JA, Thompson ID, Tolhurst DJ.** Spatial summation in the receptive fields of simple cells in the cat's striate cortex. *J Physiol* 283: 53–77, 1978.
- Murthy A, Humphrey AL, Saul AB, Feidler JC.** Laminar differences in the spatiotemporal structure of simple cell receptive fields in cat area 17. *Vis Neurosci* 15: 239–256, 1998.
- Nishimoto S, Gallant JL.** A three-dimensional spatiotemporal receptive field model explains responses of area MT neurons to naturalistic movies. *J Neurosci* 31: 14551–14564, 2011.

- Nowak LG, Azouz R, Sanchez-Vives MV, Gray CM, McCormick DA.** Electrophysiological classes of cat primary visual cortical neurons in vivo as revealed by quantitative analyses. *J Neurophysiol* 89: 1541–1566, 2003.
- Oliver M.** *Spatio-temporal receptive field lab (STRFlab)*. <http://strflab.berkeley.edu/>, 2010.
- Olmos A, Kingdom FA.** *McGill Calibrated Colour Image Database*. <http://tabby.vision.mcgill.ca>, 2004.
- Olshausen BA, Cadieu CF, Warland DK.** Learning real and complex overcomplete representations from the statistics of natural images (Abstract). *Proc SPIE* 7446: 7470S, 2009.
- Olshausen BA, Field DJ.** Natural image statistics and efficient coding. *Network* 7: 333–339, 1996.
- Olshausen BA, Field DJ.** How close are we to understanding V1? *Neural Comput* 17: 1665–1699, 2005.
- Petrusca D, Grivich MI, Sher A, Field GD, Gauthier JL, Greschner M, Shlens J, Chichilnisky EJ, Litke AM.** Identification and characterization of a Y-like primate retinal ganglion cell type. *J Neurosci* 27: 11019–11027, 2007.
- Pettersen KH, Devor A, Ulbert I, Dale AM, Einevoll GT.** Current-source density estimation based on inversion of electrostatic forward solution: effects of finite extent of neuronal activity and conductivity discontinuities. *J Neurosci Methods* 154: 116–133, 2006.
- Priebe NJ, Mechler F, Carandini M, Ferster D.** The contribution of spike threshold to the dichotomy of cortical simple and complex cells. *Nat Neurosci* 7: 1113–1122, 2004.
- Rehn M, Sommer FT.** A network that uses few active neurons to code visual input predicts the diverse shapes of cortical receptive fields. *J Comput Neurosci* 22: 135–146, 2007.
- Reid RC, Soodak RE, Shapley RM.** Directional selectivity and spatiotemporal structure of receptive fields of simple cells in cat striate cortex. *J Neurophysiol* 66: 505–529, 1991.
- Ringach DL.** Spatial structure and symmetry of simple-cell receptive fields in macaque primary visual cortex. *J Neurophysiol* 88: 455–463, 2002.
- Ringach DL, Shapley RM, Hawken MJ.** Orientation selectivity in macaque V1: diversity and laminar dependence. *J Neurosci* 22: 5639–5651, 2002.
- Schiller PH, Finlay BL, Volman SF.** Quantitative studies of single-cell properties in monkey striate cortex. I. Spatiotemporal organization of receptive fields. *J Neurophysiol* 39: 1288–1319, 1976.
- Skottun BC, Valois RL, Groszof DH, Movshon JA, Albrecht DG, Bonds AB.** Classifying simple and complex cells on the basis of response modulation. *Vision Res* 31: 1079–1086, 1991.
- Song Y, Baker CL Jr.** Neural mechanisms mediating responses to abutting gratings: luminance edges vs. illusory contours. *Vis Neurosci* 23: 181–199, 2006.
- Swindale NV.** Orientation tuning curves: empirical description and estimation of parameters. *Biol Cybern* 78: 45–56, 1998.
- Talebi V, Baker CL Jr.** Natural versus synthetic stimuli for estimating receptive field models: a comparison of predictive robustness. *J Neurosci* 32: 1560–1576, 2012.
- Tanaka H, Ohzawa I.** Surround suppression of V1 neurons mediates orientation-based representation of high-order visual features. *J Neurophysiol* 101: 1444–1462, 2009.
- Troyer TW, Krukowski AE, Priebe NJ, Miller KD.** Contrast-invariant orientation tuning in cat visual cortex: thalamocortical input tuning and correlation-based intracortical connectivity. *J Neurosci* 18: 5908–5927, 1998.
- Vigneswaran G, Kraskov A, Lemon RN.** Large identified pyramidal cells in macaque motor and premotor cortex exhibit “thin spikes”: implications for cell type classification. *J Neurosci* 31: 14235–14242, 2011.
- Vinje WE, Gallant JL.** Sparse coding and decorrelation in primary visual cortex during natural vision. *Science* 287: 1273–1276, 2000.
- Vinje WE, Gallant JL.** Natural stimulation of the nonclassical receptive field increases information transmission efficiency in V1. *J Neurosci* 22: 2904–2915, 2002.
- Willmore BD, Prenger RJ, Gallant JL.** Neural representation of natural images in visual area V2. *J Neurosci* 30: 2102–2114, 2010.
- Wilson CJ, Kawaguchi Y.** The origins of two-state spontaneous membrane potential fluctuations of neostriatal spiny neurons. *J Neurosci* 16: 2397–2410, 1996.
- Worgotter F, Eysel UT.** Quantitative determination of orientational and directional components in the response of visual cortical cells to moving stimuli. *Biol Cybern* 57: 349–355, 1987.
- Wu MC, David SV, Gallant JL.** Complete functional characterization of sensory neurons by system identification. *Annu Rev Neurosci* 29: 477–505, 2006.
- Xing D, Ringach DL, Hawken MJ, Shapley RM.** Untuned suppression makes a major contribution to the enhancement of orientation selectivity in macaque V1. *J Neurosci* 31: 15972–15982, 2011.
- Xing D, Yeh CI, Shapley RM.** Spatial spread of the local field potential and its laminar variation in visual cortex. *J Neurosci* 29: 11540–11549, 2009.
- Zheng L, Yao H.** Stimulus-entrained oscillatory activity propagates as waves from area 18 to 17 in cat visual cortex. *PLoS One* 7: e41960, 2012.
- Zhou YX, Baker CL Jr.** Envelope-responsive neurons in areas 17 and 18 of cat. *J Neurophysiol* 72: 2134–2150, 1994.